UNCLASSIFIED

AD **258 009**

Reproduced
by the

ARMED SERVICES TECHNICAL INFORMATION AGENCY
ARLINGTON HALL STATION
ARLINGTON 12, VIRGINIA

UNCLASSIFIED

DISCLAIMER NOTICE

UNIVERSITY OF MINNESOTA
INSTITUTE OF TECHNOLOGY
ROSEMOUNT AERONAUTICAL LABORATORIES

Experimental Investigations of Laminar Heat Transfer and Transition with Foreign Gas Injection — A 16° Porous Cone at M = 5

Minneapolis 14, Minnesota
October 1960

Copy No. 18

UNIVERSITY OF MINNESOTA
INSTITUTE OF TECHNOLOGY
ROSEMOUNT AERONAUTICAL LABORATORIES

EXPERIMENTAL INVESTIGATIONS OF LAMINAR HEAT TRANSFER AND TRANSITION WITH FOREIGN GAS INJECTION - A 16° POROUS CONE AT M = 5

by
C. J. Scott

Minneapolis 14, Minnesota
October 1960

ASTIA

JUN 22 1961

TIPDR

APPROVED: John D. Akerman

Professor John D. Akerman, Director
Rosemount Aeronautical Laboratories

BIBLIOGRAPHICAL CONTROL SHEET

1. Originating Agency and Monitoring Agency:
   O.A.: Rosemount Aeronautical Laboratories, University of Minnesota
   M.A.: Mechanics Division, Office of Scientific Research.

2. Originating Agency and Monitoring Agency Report Number:
   O.A.: Rosemount Aeronautical Laboratories, University of Minnesota
         Research Report No. 174.
   M.A.: AFOSR TN-60-1370.

3. Title and Classification of Title:
   "Experimental Investigations of Laminar Heat Transfer and Transition With
   Foreign Gas Injection - A 10° Porous Cone at M = 5" (UNCLASSIFIED).

4. Personal Author: C. J. Scott

5. Date of Report: October 1960

6. Pages: 76

7. Illustrative Material: 36 figures (included in item 6 above).

8. Prepared for Contract No.: AF 49(638)-558

9. Security Classification: UNCLASSIFIED

10. Distribution Limitations: None

11. Abstract: Experiments on two porous 10° cones at Mach number 5 are
    discussed which present the effects of helium and nitrogen injection on
    the stability of the laminar boundary layer. Large surface cooling and
    extreme injection rates are included. Heat transfer measurements with
    these two coolants are also presented. Since the experiments neither
    confirm nor invalidate the details of the theory, special emphasis is
    placed on the discussions of experimental procedures and data reduction
    methods. Analytical estimates of the effect of the solid tip followed
    by a uniform-injection cone are presented. An analysis of the effect of
    surface mass addition on viscous boundary layer - external flow inter-
    actions is included. A correlation of data on fluid flow through porous
    media in the "slip-flow" regime is presented.

ii

NOMENCLATURE

A	area
c_p	specific heat at constant pressure
d	diameter
F	Fahrenheit
f_w	dimensionless injection parameter (Eq. A-2)
$\overline{f}_w$	dimensionless injection parameter (Eq. A-7)
k	thermal conductivity
M	Mach number
L	length of model
p	static pressure
P	total pressure
r_f	temperature recovery factor $(T_{aw} - T_\delta)/(T_U - T_\delta)$
Re	Reynolds number $(U_\delta x / \nu_\delta)$
u	velocity parallel to the surface
U	freestream velocity just outside the boundary layer
v	velocity normal to the surface
x	distance measured along ray from cone tip
μ	coefficient of dynamic viscosity
ν	coefficient of kinematic viscosity
ρ	mass density
θ	cone half angle (8°)
R,r	radius, degree Rankine
σ	Boltzmann constant 0.173×10^{-8} BTU/(hr)(ft^2)($^{\circ}$R^4)
ε_{w-m}	tunnel-model radiation interchange factor

Subscripts

,aw	condition of zero heat transfer by conduction
c	coolant
o	zero injection value, length of solid tip
t	transition
w	conditions at surface of model
δ	conditions at outer edge of boundary layer
∞	conditions in undisturbed freestream ahead of model shock wave
T	tunnel
n	nozzle
s	solid or parent material
m	measured value or coolant stagnation value
x	conditions at position x

Superscripts

†	blowing rates defined in Equation (A-2) multiplied by the factor $\sqrt{1 - \dfrac{x_o}{x}}$.
*	conditions at sonic orifice
–	uniform injection mass flux

iv

INTRODUCTION

Mass effusion methods are currently being utilized for protecting surfaces exposed to intense forced convective heating, a problem which occurs in many new engineering applications. In particular, the application of effusion cooling methods to the forward areas of high-speed aircraft and missiles has stimulated research on the basic processes of these cooling techniques.

The primary characteristic of the several proposed methods is that a mass flow of gas away from the surface simultaneously influences the development from the velocity, temperature, and diffusion boundary layers. This feature distinguishes effusion techniques from conventional cooling methods which depend on either a high thermal capacity heat sink within the structure or a heat pump system located at the inner surface of the skin. The coolant may be a gas, or a solid or slurry which decomposes to form a gas, or a liquid which forms a film on the surface and eventually evaporates into the boundary layer.

Film cooling maybe described as the injection through a porous strip or slot of a liquid or gas which blankets the solid surface downstream of it. Transpiration cooling refers to the injection through an extended porous surface of a gas which has the same thermodynamic properties as the main stream. Mass transfer cooling is similar to transpiration cooling except the coolant has thermodynamic properties differing sufficiently from the exterior stream so that the diffusion process must be taken into account.

Since all surface effusion cooling techniques have the common feature of a mass flow of a coolant gas flowing away from the surface to be cooled, porous wall experimental investigations are of general interest since this effect is isolated and controllable. Porous wall mass transfer cooling requires the pumping of a coolant through a porous surface. Such a system is basically efficient because: (1) the flow passages within the porous skin possess a large surface area and are extremely tortuous, providing an efficient heat exchange between the coolant and the skin; and (2) simultaneous injection and diffusion phenomena significantly reduced the amount of heat entering the body. In addition to the attractive possibility of significantly lowering the heat inputs and equilibrium temperatures of the body, the laminar stability of the boundary layer may be altered by modifications of the flow profiles and the boundary layer fluid properties.

The thermal properties of gases depend primarily on the molecular weight. It has been shown that the surface friction and heat transfer characteristics are quite different when the injected coolant gas has properties differing widely from the main flow. For these reasons nitrogen and helium were used as the coolant gas because these choices result in molecular weight ratios of approximately 1:1 and 1:7 when compared to air.

1

This paper presents an extension of the experimental research work on mass transfer cooling effects carried out at the Rosemount Aeronautical Laboratories during the last few years. The present results include extended investigations of the laminar stability with nitrogen and helium injection and an experimental investigation of these coolants on the heat transfer characteristics of a 16° conical model at a freestream Mach number of 5.

OUTLINE OF CURRENT INVESTIGATIONS

There were two principal objectives to the current work. An initial UMRAL investigation of the thermal effects of gaseous injection on the stability of the covering laminar boundary layer was restricted to helium injection at a single injection rate[3]. In the present investigation this was expanded to include nitrogen injection and cover a more complete range of wall-to-stagnation temperature ratios for both coolant gases. In another previous UMRAL investigation of heat transfer characteristics the range of blowing rates used was restricted by the apparatus to rather moderate levels[4]. It was the purpose of the second portion of this investigation to extend the range of blowing rates to include the entire range of interest. Turbulent flow investigations were excluded because of the lack of effective turbulence trips at Mach number 5.

BOUNDARY LAYER TRANSITION WITH GAS INJECTION

In any practical aerodynamic application, a great uncertainty lies in predicting and controlling the location of the boundary layer transition. One must rely wholly on available experimental information and therefore on the probability of finding data applicable to the situation. Only the subsonic data of Reference 5 and the preliminary UMRAL studies (Reference 3) existed at the outset of this program. This pair of data agreed qualitatively as to the destabilizing effects of injection but disagreed markedly as to the magnitude of the effect(s). The question arises as to whether extensive regions of laminar flow can exist with finite injection rates through structural suitable porous plates. The surface roughness of such materials may prove to be an obstacle - in certain situations the existence of discrete jets of coolant issuing from the finite opening may produce premature transition. Experimentally one finds that a relatively sharp transition from laminar to turbulent flow still takes place when injection is utilized and that this pattern oscillates on the surface. One feels the transition must be governed by the detailed character of the flow which is related to the history of the fluid particles as they progress into the transition region, and, therefore, must be sensitive to the distributed nature of such disturbances.

The mathematical model of transition is anything but secure at present. The Tollmien-Schlichting theory of laminar boundary layer instabilities[6,7] has been proposed as one mechanism leading eventually to

Transition. It is postulated that very small 2-dimensional disturbances will be amplified selectively according to frequency if the flow Reynolds number is high enough. The large oscillations produced may interact and the flow will be broken up into turbulent vortices. The analysis is unable to predict the Reynolds number of transition from laminar to turbulent flow because of limitations on the equations of motion used. The most interesting point of practical importance in connection with this analysis is the predicted existence, within a certain Mach number and surface temperature range, of a completely stable laminar boundary layer[8]. One must regard the quantitative results of stability analyses with caution since the analysis has been linearized and is based on small 2-dimensional disturbances. In reality, supersonic wind tunnels and conical models may generate disturbances which are neither small nor 2-dimensional. The analysis of Dunn and Lin[9] indicates that for 3-dimensional disturbances, cooling should increase the transition Reynolds number but no region of infinite stability was found to exist.

Low speed experiments on porous flat plates revealed that mass addition has a significant effect on producing premature transition[5,10]. Since fluid injection has a destabilizing effect, while surface cooling appears to be stabilizing, it is important to perform stability calculations to determine which effect is dominant. Low[11] and others[12,13] have performed the calculations for air injection using the stability equations of Dunn and Lin[14]. The results show that the surface must be cooled to lower surface temperatures in order to obtain complete stability as the injection rate is increased. Baron[15] and Covert[16] have estimated binary stability limits for air, helium, and carbon dioxide injection which reveal qualitatively the same results. That is, at moderate Mach numbers, the required surface temperatures for complete stabilization with the injection of air, helium, and carbon dioxide are, in general, slightly lower than the solid surface requirement calculated by van Driest[17].

In Reference 3, work done at the Rosemount Aeronautical Laboratories revealed that at zero heat transfer, the observed transition Reynolds numbers do decrease with increased injection, (initially more rapidly for helium than for air), but the percentage decreases are not large for injection rates which theoretically produce significant coolant effects. In that study attempts to investigate the effects of extremely low temperature air injection upon boundary layer transition failed because of water vapor condensation in the coolant ducts. This problem was eliminated in the present studies through the use of dry nitrogen.

3

EXPERIMENTAL FACILITY

The compressed air installation consists of five parallel-connected, electrically-driven, reciprocating, 2-stage air compressors with a total rating of 3800 horsepower which have a maximum delivery rate of 23.2 pounds per second at 110 psig. The vacuum system consists of seven rotary-vane pumps driven by four 250 horsepower induction motors. Compressed air for the wind tunnel can be routed through an electric heater bank to provide stagnation temperatures up to $430^\circ F$ at 11 pounds per second. The supersonic continuous wind tunnel has a 6 x 9-inch test section with a Mach number range of 1.5 to 5.7 (Figure 1). At a Mach number of 5, it operates continuously over a Reynolds number per inch range of 0.14×10^6 to 0.91×10^6. The tunnel is equipped with a variable-area diffuser with three throat positions. The total temperature of the air stream is sensed by seven thermocouples in the stagnation chamber. The tunnel is equipped with rectangular optical windows 14-1/2 x 6-inches in size. During the present investigation the wind tunnel was relocated in a new building designed specifically for combustion work. This was done in order to extend the mass transfer studies to include hydrogen injection with combustion. Thus, the new building was designed with particular emphasis on the safety of the operating personnel. The building contains a wind tunnel, a combustion test cell, and two control rooms (Figure 2). Reinforced concrete walls separate the tunnel cells from the control rooms and Herculite glass 1-1/4-inch thick is used as viewing ports. One wall and the roof of each cell is of light construction, facilitating easy blow-off in the event of an explosion. Further details of the facility are available in References 1 and 2.

The 16° Porous Cone - Transition Model

The porous test model used in this investigation (Figure 3) was a 16° cone of sintered type 316 stainless steel powder (5 micron particle stoppage). The average wall thickness was 0.028-inch. The cone had a solid steel tip one inch long. The model slant height was 14.7-inches and had a base diameter of 4.1-inches. The density of the cone surface material was approximately 245 pounds per cubic foot with an average relative density of 0.55. Of a total cone surface area of 0.660 square feet, 0.635 square feet was porous. The cone shell was fabricated by Connecticut Metals, Incorporated, Meriden, Connecticut. The permeability distribution was built into a flat sheet of 10 x 21-inch dimensions through the use of contoured dies. The sheet was sintered, cross-rolled, and pressed to obtain a smoother outside surface, and resintered. The finished sheet was rolled into its final conical shape using standard sheet metal forming techniques and welded along a single ray. The 3/16-inch seam was hand finished to conform to the conical contour. A 3-inch circular sector porous insert was required to complete the contour (Figure 4).

4

the concentricity of the model as indicated by a dial gage on the circumference, while the cone was rotated about its axis, was found to be within ± 0.010 inch. The average roughness height as measured by a profilometer on the model was found to vary from 7 microinches at the base to 30 microinches at the nose. This variation is due to the imposed permeability distribution being compact near the base (Figures 6a,6b). These surfaces are comparable to a production grind finish. The permeability distribution of this cone was carried out by Mr. R. Rokower of the Massachusetts Institute of Technology, using a test probe with an area of 0.197 inch and an average pressure differential of 8 inches of water at atmospheric exhaust. The results are presented as Figures 6a,6b. In order not to disturb the imposed permeability distribution, the instrumentation was kept at a minimum. Two individual (.002 × .030-inch) copper-constantan thermocouples were inserted into the exterior surface 6-3/8 inches from the tip along the two side rays. The lead wires penetrated the porous skin through ceramic insulation and were hermetically sealed at the rear of the insulations. Two pressure taps were installed on the same side rays 6 inches from the tip. The welded seam was located 90 degrees from the viewed rays.

Phase A helium and oil-pumped nitrogen were injected through the porous surface. The gases were filtered prior entering the model by means of a porous stainless steel filter 1/4-inch thick. An examination of the model after extensive testing revealed no dirt particles or appreciable discoloration on the inner surface of the porous cone. This point was pursued further by examining a similar porous model investigated extensively in Reference 5. This model was sawed in half and the interior was inspected with a microscope – with similar results. Therefore, it is believed that no significant permeability variations were introduced as a result of accumulation of matter within the porous surface.

The afterbody of the model was cast from polyester foam which enclosed the cooling jacket and vacuum system. The afterbody took the shape of a cone, similar in shape to the frontal cone and was formed from a sheet of 30-mill brass shim stock. The liquid was poured through the apex of the afterbody cone and permitted to react chemically until the foam filled the entire afterbody. This method of construction is cheap and provides excellent thermal insulation of the coolant supply ducts.

A 27 cylinder manifold, used alternately for helium or nitrogen bottles, served as a coolant reservoir. A pressure regulator and a calibrated sonic orifice were used to regulate and measure the coolant mass flow. A parallel system of liquid-gas heat exchangers was used to control the coolant temperatures. The coolant section contained a carbon dioxide bath precooler and a liquid nitrogen bath cooler. The heater section contained a copper coil inserted in an electrically heated water bath. Coolant gas temperatures could be varied between boiling water and liquid nitrogen temperatures by using a parallel valve system. Between the cooler and sonic orifice (located within the cone 6 inches from the base) the supply tubing was double-walled,

permitting an external vacuum jacket. The heat exchanger, supply
tubing, and sonic orifice were used for both the transition and
heat transfer studies. Aluminum safety discs were installed in
the system to prevent the pressure build-up resulting from the
evaporation of the liquid nitrogen formed inside the coils of the
liquid nitrogen bath.

Since gaseous nitrogen was used in connection with a liquid
nitrogen bath, some of the gaseous nitrogen was liquified in passing
through the bath at higher pressures. The maximum stagnation pressure
of the mass flow orifice was restricted to slightly below atmospheric
pressure. With a fixed maximum injection rate, the orifice diameter
could then be determined. The actual orifice diameter (d = 0.150-inch)
was measured to ± 0.001-inch with a 20x microscope equipped with a
calibrated reticule.

The flow meter stagnation temperatures could be set to within
5 degrees of any desired temperature between 200°F and -300°F. The
temperature could then be maintained to within one degree of the set
value through the run. Control of the flow meter stagnation pressure
was obtained by the use of a parallel set of fine-thread, linear-
control, needle valves. This valve-staging system allowed control
of the coolant supply pressure to ± 0.05-inches of mercury throughout
each run.

The photographic observations employed an AIRCON double path
schlieren system. Flash durations of 1 microsecond were used with
the E.G.F. x 12 flash lamp. Intensity variations were possible
due to the two spark capacitors of 0.1μF and 0.5μF.

Preliminary Results

Actual detection of transition was by inspection of full-size
shadowgraph photographs. This technique proved to be more successful
than using enlarged double-path schlieren photographs. A compromise
had to be made between the tunnel stagnation pressure (to be maximized
in this case if the density profile curvature is to be observed with
a shadowgraph) or minimized (to produce the maximum length of laminar
flow along a conical surface). The tunnel Reynolds number per inch
selected was 0.36×10^6 which did not permit the maximum length of
laminar flow along the model. Nearly true size model images resulted.
The use of a 11 x 14-inch X-ray film and Kodabromide-5 high contrast
photographic paper resulted in easily read prints. Using these
techniques the error in transition location - x_t - is felt to be
less than ± 1/2-inch. Typical shadowgraphs showing transition appear
in Figures 5a-5d. Interesting excess injection phenomena are also
presented which show the conical shock wave being deformed by boundary
layer thickening due to surface injection (see appendix C). Transition

6

is taken to occur at the end of the white line which appears just above the surface in the laminar region. Attempts were made to employ the technique employed by Chapman in Reference 18 which magnified the distance between the white line and the model surface. The film plane was moved away from the tunnel at several positions but the moderate success obtained did not warrant the additional expenditures required to improve the technique. The zero injection transition position was found to be approximately 10-inches, depending somewhat on model surface temperatures. Four separate shadowgraph photographs were taken at each blowing rate condition. The photographs were read independently by two observers and the results averaged. An expanded discussion of the accuracy of this method of transition detection is presented in Reference 3.

Transition Results

The two surface static pressure taps indicated a nominal surface Mach number of 4.33 at a tunnel Reynolds number per inch of 0.38×10^6. This is to be compared with a calculated surface Mach number of 4.42. This fact is to be of importance during the heat transfer measurements described in the next section. An increase of surface static pressure with injection rate was noted (probably due to the increased boundary layer displacement thickness) but this effect was not documented sufficiently to be included in the data reduction procedures (see Appendix C for an expanded discussion).

Because of the wide range of variables involved, and in the interest of economy, the data was not taken under truely steady-state surface temperature conditions. After the coolant flow rate and temperature were set at the desired values, the model surface temperature was allowed to adjust itself for a period of approximately five minutes before the shadowgraph photographs and temperature-pressure data were taken. Although the 0.028-inch wall thickness model was very rapid in thermal response, some temperature drift did occur.

A complete presentation of the nitrogen data is presented as Figures 7 and 8. Figure 7 reveals the major effect, the reduction in transition Reynolds number with injection rate. The effect of surface temperature variation is shown more clearly in Figures 8a-8f and is summarized in Figure 9. The stabilizing effects of surface cooling are seen to exist up to blowing rates of 1.0. At the higher blowing rates the effect of cooling is seen to diminish and even reverse at the highest blowing rate, $f_w = 3$, presented. It must be pointed out that the blowing rates presented here encompass the complete range of aerodynamic interest - the somewhat questionable theoretical blow-off value being about 2. Within this range the transition Reynolds number is seen to decrease only about 50 percent, depending only to a slight degree on surface heat transfer conditions. It will be shown in the next section that the heat transfer coefficients are simultaneously reduced by nearly 90 percent. In Figure 10 the present nitrogen data are compared with other available experimental results[3,19]. The agreement can be considered favorable considering the apparatus and

7

elusive nature of transition measurements. Figures 11 through 13
present corresponding results for helium injection. No major
differences appear between the nitrogen and helium results. The
observed transition Reynolds numbers initially decrease somewhat
faster per unit injection rate for helium than for nitrogen but the
results for both gases asymptotically approach the same transition
position.

HEAT TRANSFER INVESTIGATIONS

Porous 16° Cone

The test body used in the heat transfer investigations was
identical in all geometric features to the transition model (Figure 14).
The porous cone permeability distribution was measured using the
calibration apparatus represented schematically in Figure 15. The
cone was fastened to a rigidly held mandrel. The manipulator was
used to position the surface probe at the desired location on the
model surface. The internal diameter of the sharp-edged surface
probe was 1/8-inch. Air was injected into the model through an
orifice located downstream of a pressure regulator and valve. A
soap solution diaphram was formed on the open bell and stabilized
by adjustment of the needle valve upstream of the vacuum line.
(Stabilizing the diaphragm refers to flow at atmospheric pressure,
eliminating restricting effects the probe may impose on the flow
because of its proximity with the cone surface.) When the open bell
diaphragm was stabilized, a soap solution diaphragm was formed on
the base of the calibrated tube and its rate of ascent in the tube
was measured. The reading was recorded and the vacuum needle valve
was then used to destabilize the open bell diaphragm and again
stabilize it as a precautionary measure to insure against errors
due to soap drying on the open bell. A total of three readings
were taken in this manner and were averaged to give one value for
the given probe location. It is felt that this procedure is justified
since the three readings varied by at most $\pm$ 3 per cent. The probe
was then moved to the next position along the cone ray and the procedure
repeated. After completion of the measurements along a ray, the cone
was rotated on the mandrel, positioning another ray under the probe.

It must be pointed out here that calibrations of this type give
qualitative evidence only. The use of larger diameter surface
probes always decrease the "apparent scatter" of the data while
a smaller probe will magnify scatter up to the point where individual
pore openings are being sensed. A general description of the
permeability distribution (in the spirit of best effort) is all that
can be hoped for.

8

It is seen that in figures 16a through 16g the actual permeability distribution approximates the theoretical one which requires an inverse variation with the square root of x. The problem of obtaining the proper permeability distribution is the most vexing obstacle to injection cooling experiments. Once this is achieved, the primary problem is to generate either a constant external surface pressure or one which is small compared to the pressure drop across the porous surface. A combination of high tunnel Mach number, low tunnel stagnation pressure, and small cone angle was used to develop the second condition. The pressure drop across the porous surface approaches zero with the injected flow rate so that effects of external pressure variations should diminish with increased injection rate. The low densities which resulted from this combination of variables produced a rather unexpected result — the flow of coolant through the porous surface was governed by a "slip flow" phenomena because of the increased mean free path and small characteristic length of the porous media. (See Appendix D for an expanded discussion of this effect.)

The top ray of the cone had eleven thermocouples positioned one inch apart while the bottom ray had ten stations one inch apart. A 0.030-inch hole was drilled, and the outer surface "Spot Faced" 0.050-inch in diameter by 0.004-inch deep. A 0.003-inch thick brass shim stock disc was soft-soldered into the surface recess. Two 0.004-inch holes were drilled into the shim stock and the copper-constantan thermocouples soft-soldered to the shim-stock disc. A double-hole ceramic rod was cemented into the remaining hole in the surface. A 36 gage id = 0.005-inch premium grade copper-constantan thermocouple was forced through the ceramic rod, soldered to the shim-stock, and hand finished. This procedure established a definite thermal contact with the outside surface only. Since five diameters of ceramic rod extended into the cone interior some additional insulating value was gained which tended to reduce lead wire heat conduction while the cement permitted no coolant leakage around the plug. There were no pressure taps installed in this model. Coolant thermocouples were tied to the lead wire of the surface thermocouples every two inches and located approximately 1/4-inch from the inner surface of the cone. This pairing of thermocouples permitted a measure of convective heat transfer to the surface due to the coolant q. These thermocouples were connected through a 48-unit manual switching unit through a variable-speed Minneapolis Honeywell continuous temperature recorder equipped with a -350 to +150°F copper-constantan calibration. The average accuracy of the temperature measurements is +1.5°F. Measurements of 22 surface temperatures, 11 coolant temperatures 7 tunnel stagnation temperatures, one coolant mass flow stagnation temperature, and ice water, and liquid nitrogen reference bath temperatures were obtained using this recorder. The data gathering procedure generally required about three minutes time per injection rate.

The instrumented porous cone model was first run with zero coolant injection to obtain the distribution of the recovery factors at two tunnel total pressures (figure 17). At a tunnel Reynolds number per inch of

9

0.33×10^6 the transition position is found to vary from x = 7 to x = 9 inches from the tip of the cone, indicating rather poor rotational symmetry. This condition duplicated the transition experimental runs. The decrease in transition position from a value of 10 inches on the transition model is undoubtedly due to the thermocouple installations. For the heat transfer runs, the tunnel total pressure was cut in half in order that fully laminar flow could be obtained on the porous cone under the conditions of zero coolant injection as verified by the recovery factor data in Figure 17. Because of the lower tunnel densities, the shadowgraph photographs were not as definitive in locating the transition position as in the transition studies; and here the zero injection transition position as indicated by shadowgraphs was seen to fall on the test surface. Since the recovery data and shadowgraphs disagree at the lower tunnel densities, the shadowgraph method of determining transition is not considered adequate at the lower density level. In order to get some estimate of the radiation correction, and its variation with axial position, the recovery factors were corrected for thermal radiation, as described in Appendix A, with the results presented in Figure 18. Qualitatively the recovery factors seemed to decrease, more for the rearward positions, and agree well with the theoretical square root of Prandtl number predictions. A summary of the transition data on the heat transfer model is presented for reference in Figures 19 and 20.

The final heat transfer runs consumed a total of 28 tunnel running hours. The nitrogen data was taken first and required six hours on the first day and seven hours on the second day. The helium data was taken during the span of one fifteen hour operating day.

The basic experimental procedure employed is as follows: supersonic flow was established in the wind tunnel and the tunnel stagnation pressure adjusted to provide the proper free-stream-Reynolds-number-per-inch of 0.18×10^6. The desired coolant mass flow was established. The coolant temperature was adjusted to the desired value and the coolant mass flow stagnation pressure re-adjusted to provide the desired flow rate (see Appendix A). The system was allowed to stabilize re-adjusting the flow and temperature conditions when necessary. A minimum of twenty-five minutes was required to obtain thermal equilibrium. After a set of measurements had been taken the coolant mass flow temperature was changed and the coolant mass flow stagnation pressure re-adjusted to provide the identical blowing rate. Generally, seven different surface temperature levels were studied. Because of the thermal losses between the coolant bath and the model the range of temperatures increases with the coolant mass flow.

A typical set of surface and coolant temperature distributions is shown in Figures 21a through 21d. The open symbol represents surface temperatures and the closed represent coolant temperatures. The data presented is for helium injection along the bottom ray of the cone. Some of the temperature data were not used in the heat transfer coefficient calculations because of the large inaccuracies associated with small temperature differences. The surface temperatures are seen to be reasonably smooth - indicating a relatively smooth blowing distribution. The coolant temperature distribution closely follows the surface temperatures. These two are intimately related. The variation of coolant temperature with axial location indicates that there is a considerable amount of mixing occurring within the interior of the porous cone. The surface temperatures are seen to become more nearly uniform as the injection rate is increased. One may conclude that either the blowing distribution is changing or the effect of the solid tip diminishes with increased injection. The only results giving reasonable variations with x were found by using a constant surface injection mass flux. The injection parameter f_w' includes the factor $\sqrt{1 - x_o/x}$ which properly accounts for the solid leading edge[26]. A typical result of these calculations is presented in Figure 22 which presents the data for a moderate helium injection rate of $f_w = 0.50$. The injection parameter f_w employs the constant injection mass flux. The significant features of Figure 22 are that the radiation correction is only 15 percent of the injected heat flux and that the surface heat conduction is less than 1 percent of the surface heat flux. Since the surface temperature distribution was approximated by a series of linear segments for the variable surface temperature correction, the first position necessarily indicates a heat flux which is 62 percent higher than that predicted by constant surface temperature theory at that surface temperature[27,28]. The variable surface temperature correction is seen to diminish from 1.62 at the first thermocouple station down to approximately 1.01 at the sixth thermocouple station. This correction reduces the measured surface heat flux.

The slope of a heat flux versus wall temperature plot is proportional to the heat transfer coefficient h while the temperature intercept defines the recovery temperature T_{aw}. If the temperature differences are small this curve should be a straight line (see Figure 23). Theoretically, the surface heat flux and the heat transfer coefficient should each vary inversely with the square root of x as does the surface mass flux. Dividing the calculated h values by h_o should yield a ratio which is independent of x.

A possible explaination for the high heat transfer values near the tip is that there is a pressure gradient external to the model which affects the blowing distribution (see Appendix C). Since no pressure taps were installed in the model this effect could not be verified. The data (temperature distributions and heat flux distributions) indicate that at relatively low injection rates the blowing velocities increase from zero at the leading edge for the first 4-inches and then remain constant.

11

Another approach to this problem is to assume that one can measure the distribution of heat transfer coefficients more accurately than he can apply calibrated permeability distributions to the wind tunnel conditions. In this case, one would find that the blowing distribution would start at zero at the leading edge of blowing increase for the first four inches and then remain constant. This concept seems to be reasonably close to what has happened. At any rate, the data was reduced assuming the blowing velocity to be constant.

Figure 24 represents a calculation of the reduction of heat transfer coefficients with injection along the bottom ray of the porous cone. The first and second thermocouple positions consistently produced high heat transfer coefficients. This effect is probably due to an over-estimation of the injection rates ($p_w v_w$) in the vicinity of the tip. The data indicates that the proper distribution must increase slowly for the first four inches of porous surface. Behind this region the injection rate is then sensibly constant. Except at the first and last thermocouple stations, the reduction in heat transfer coefficients seems to be uniform along the surface of the porous cone. The data presented for $x = 5.2$ is somewhat lower than the rest. This may be explained by the fact that this coolant temperature had to be calculated from adjacent coolant temperatures. This thermocouple is located at a position where both the surface temperature and the coolant temperature profiles have abrupt changes in curvature. Only the positions $x = 2.2$, 4.2, 6.2 and 9.2 inches possess measured coolant temperatures while the remainder requires that coolant temperature values be obtained from faired curves. The first thermocouple was omitted in the subsequent plots because of the assumption of a linear variation between the first measured temperature and the nose temperature (assumed to be equal to the recovery temperature as calculated by square root of the Prandtl number). The last thermocouple was omitted in the subsequent plots because of the onset of transition at the higher blowing rates.

Figures 25 through 28 present a summary of the heat transfer data. The points above an h/h_o of unity reveal the discrepancy between the measured results and the well-verified theory of Chapman and Rubesin[24] and the over-estimation of the blowing rate near the leading edge of blowing. At the larger blowing rates the data decrease monotonically in a fashion roughly paralleling the theoretical predictions of Low (which is actually for air to air systems) and Baron (helium-air) as explained in Appendix B. For nitrogen injection along the bottom ray the last thermocouple appears transitional in the shadowgraphs and surface temperature traces. The next higher blowing rate point at this position (not plotted) is definitely transitional - having an h/h_o value of 1.3.

12

A summary of the temperature recovery factor data is presented in Figure 29. Contrary to the theoretical predictions of recovery factor, which decrease with increasing injection, the experimental values increase with blowing rate. An explanation for this phenomena has not been advanced.

At the highest blowing rates the character of the flow is markedly different than that postulated by the analysis. The reader is again referred to Figures 5a through 5e.

---

*During the publication of this report, a private discussion with Dr. E. R. G. Eckert of the Heat Transfer Laboratory of the University of Minnesota revealed that their theoretical calculations on hydrogen injection along a flat plate at freestream temperatures comparable to those in the present experimental investigation predict an increase in temperature recovery factor with injection. This effect does not continue to exist at freestream temperatures comparable to atmospheric or higher.

APPENDIX A

DATA REDUCTION PROCEDURES

The quantities measured during each run are listed in the following table:

$T_w(x)$	the external surface temperatures
$T_c(x)$	the internal, or coolant supply temperature
T_n	the nozzle wall temperature
T_f	the tunnel stagnation temperature
T_m	the coolant meter stagnation temperature
p_f	the tunnel stagnation pressure
p_m	the coolant meter stagnation pressure
x_f	transition location.

Other data determined from preliminary investigations include:

$\rho_w v_w(x)$	the measured injection mass flux distribution
$\sigma \epsilon (x)$	radiation factors for the exchange of radiant energy between the model surface and the test section walls (nozzle and porous surface emissivity).
$k(x)$	the thermal conductivity of the porous material
t	the porous surface thickness

and, in addition model and coolant meter dimensions and constants derived from the surface Mach number (4.33) of the conical flow field.

Heat Balance

14
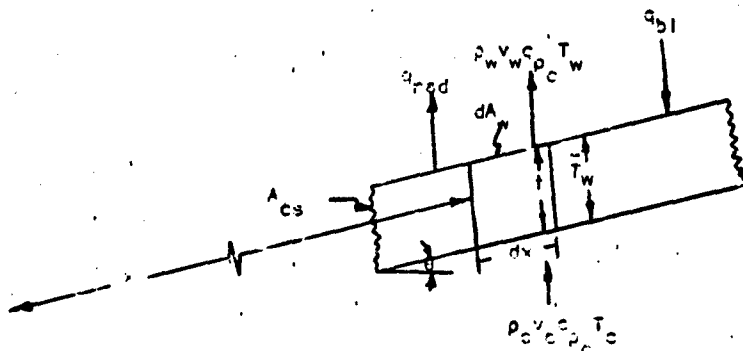
The general heat balance may be written:

$$q_{b1}dA_w = \rho_f v_f c_{p_f} T_f dA_w - \rho_c v_c c_{p_c} T_c dA_w$$

$$+ kA_{cs}\left[\frac{\sigma\bar{T}_w}{dx} - \frac{d\bar{T}_w}{dx} + \frac{d^2\bar{T}_w}{dx^2}\ dx\right] + \sigma\epsilon_{w-n}(T_w^4 - T_n^4), \qquad \text{(A-1)}$$

where
$$dA_w = 2\pi x \sin\theta\ dx; \quad A_{cs} = 2\pi xt \sin\theta.$$

From mass continuity,
$$\rho_f v_f = \rho_c v_c = \rho_w v_w\ .$$

Assuming
$$c_{p_f} = c_{p_c},\ T_f = T_w = \bar{T}_w , \qquad\qquad\qquad \text{(A-2)}$$

we arrive at the resulting heat balance:

$$q_{b1} = h(T_{aw} - T_w) = \rho_w v_w c_{p_c}(T_w - T_c) - kt\frac{d^2 T_w}{dx^2} + \sigma\epsilon_{w-n}(T_w^4 - T_n^4).$$

$$\text{(A-3)}$$

Calculation of the Surface Injection Rate When $\rho_w v_w = \dfrac{C}{x^{1/2}}$

Continuity of mass flow equates the mass flow measured at the orifice to the surface mass flow such that:

$$\rho^* V^* A^* = \int_{x_o}^{L} \rho_w v_w dA = \int_{x_o}^{L} \rho_w v_w 2\pi \sin\theta\ xdx. \qquad \text{(A-4)}$$

Defining
$$f_w = 2\frac{\rho_w v_w}{\rho_\delta U_\delta}\sqrt{\frac{\rho_\delta U_\delta x}{\mu_\delta}}\ . \qquad\qquad \text{(A-5)}$$

Taking f_w to be independent of x, Equations (A-4) and (A-5) may be combined to yield:

$$f_w = \frac{\rho^* V^* A^*}{\frac{2}{3}\pi\sin\theta\sqrt{\rho_\delta U_\delta \mu_\delta}\left[L^{3/2} - x_o^{3/2}\right]} \qquad \text{(A-6)}$$

15

The sonic mass flow is evaluated from the meter stagnation conditions in the conventional manner:

$$\rho^* V^* A^* = \frac{p^*}{RT^*}\sqrt{\gamma R T^*} \quad A^* = \left[\frac{p^*}{p_m}\sqrt{\frac{\gamma}{R}}\sqrt{\frac{T_m}{T^*}}\ \frac{\pi d^{*2}}{4}\right]\frac{p_m}{\sqrt{T_m}} \tag{A-7}$$

where the quantities in the bracket are constants for a fixed coolant gas and orifice diameter.

In a similar fashion

$$\rho_\delta U_\delta \mu_\delta = \frac{\rho_\delta}{\rho_T}\ R_\delta \sqrt{\frac{T_\delta}{T_T}}\sqrt{\frac{\gamma}{R}}\ \mu_\delta\ \frac{T}{\sqrt{T_T}} \tag{A-8}$$

Calculation of the Surface Mass Flux Assuming $\overline{\rho_w v_w}$ = Constant.

In this case

$$\rho^* V^* A^* = 2\pi\overline{\rho_w v_w}\int_{x_o}^{L} x\sin\theta\ dx \tag{A-9}$$

Defining

$$f_w = 2\ \frac{\overline{\rho_w v_w}}{\rho_\delta U_\delta}\sqrt{\frac{\rho_\delta U_\delta x}{\mu_\delta}} = \frac{\rho^* V^* A^* x}{\frac{1}{2}\pi\sin\theta\sqrt{\rho_\delta U_\delta \mu_\delta}\left[L^2 - x_o^2\right]} \tag{A-10}$$

then the relation between the two calculated f_w's is

$$\overline{f}_w = f_w\ \frac{4}{3}\left[\frac{L^{3/2} - x_o^{3/2}}{L^2 - x_o^2}\right]\sqrt{x} = .35\ f_w\ \ x(\text{inches}) \tag{A-11}$$

so that for $x \approx 9$-inches, $\overline{f}_w \approx f_w$. Each of these blowing rates were modified by multiplying by

$$\sqrt{1 - \frac{x_o}{x}}$$ to include the solid leading section effect and are signified by f_w' and $\overline{f}_w'$. (See Appendix B)

16

Sample Calculation—Nitrogen Injection

Steam and coolant conditions

a. Steam conditions

$$M_\delta = 4.33, \quad \frac{p_\delta}{p_T} = 0.02034, \quad \frac{T_\delta}{T_T} = 0.2105$$

$$\gamma_{air} = 1.4, \quad R = 1716 \; \frac{ft^2}{sec^2 - \,^\circ R}, \quad \mu_\delta \left(\frac{slugs}{ft-sec}\right) = \frac{2.270 \, T_\delta^{3/2} \times 10^{-8}}{T_\delta + 199.6}$$

b. Coolant conditions

$$\frac{p^*}{p_{o_m}} = 0.5283, \quad \frac{T^*}{T_m} = 0.8333, \quad \gamma = 1.4, \quad R = 1775 \; \frac{ft^2}{sec^2 - \,^\circ R}$$

$$d^* = 0.134\text{-inch}$$

$$f_{W_{N_2}} = 10.91 \, p_m(\text{"Hga}) \sqrt{\frac{1 + \dfrac{943.5}{T_T(^\circ R)}}{T_m(^\circ R) p_T(\text{"Hga})}}$$

For helium, $\gamma = 1.667$, $\dfrac{p^*}{p_m} = .4869$, $\dfrac{T^*}{T_T} = .7499$, $R = 12{,}432 \; \dfrac{ft^2}{sec^2 - \,^\circ R}$

$$f_{W_{He}} = 4.38 \, p_m(\text{"Hga}) \sqrt{\frac{1 + \dfrac{943.5}{T_T(^\circ R)}}{T_m(^\circ R) \, p_T(\text{"Hga})}} \tag{A-12}$$

Thermal Conductivity

Lacking exact information on the thermal conductivity of the porous material and the variation of thermal conductivity with permeability the analysis of Reference 29 was used to estimate conductivities:

$$\frac{k}{k_s} = \left[1 - p^{1/3} + \frac{p^{1/3}}{\left(\dfrac{k_c}{k_s}\right) p^{2/3} + 1 - p^{2/3}} \right]^{-1} \tag{A-13}$$

17

where

$$0 \leq P = \frac{\rho_s - \rho}{\rho_s - \rho_c} \leq 1$$

$$k_s = 11 \; BTU/ft^2 - hr - °R/ft.$$

We obtained four samples from the manufacturer which matched the permeability range of the porous heat transfer model. The relative densities (ρ/ρ_{solid}) were 0.582, 0.567, 0.532 and 0.499. Using the two extreme values only, the corresponding values of k were found to be 5.62 and 4.70 $BTU/ft^2 - hr - °R/ft$. The quantities ρ_c/ρ_s and k_c/k_s were taken to be zero. The expression

$$k \left[\frac{BTU}{ft^2 - hr - °R/ft} \right] = 4.55 + 0.0844 \; x(\text{inches}). \tag{A-14}$$

was used in the final computer data reduction program. The average thickness of the porous surface (t) was found by a series of micrometer measurements to be 0.028-inch. The surface heat conduction term was found by fitting a parabola to the temperatures at the point and its two adjacent points.

$$T_w = a + bx + cx^2 \tag{A-15}$$

such that

$$\frac{d^2T}{dx^2} = 2c, \tag{A-16}$$

where

$$c = \frac{(T_1 - T_2)(x_2 - x_3) - (T_2 - T_3)(x_1 - x_2)}{(x_1^2 - x_2^2)(x_2 - x_3) - (x_2^2 - x_3^2)(x_1 - x_2)} . \tag{A-17}$$

This procedure was also used to obtain interpolated values of the coolant temperature from the values measured at alternate stations.

Radiation Correction.

The radiation geometry may be examined by considering a cross section of the wind tunnel as shown in the following sketch:

Porous surface
$\epsilon \simeq 0.44$

Glass window
$\epsilon \simeq 0.85$

Steel sidewall
$\epsilon = 0.3$

Chrome plated
nozzle $\epsilon \simeq 0.07$
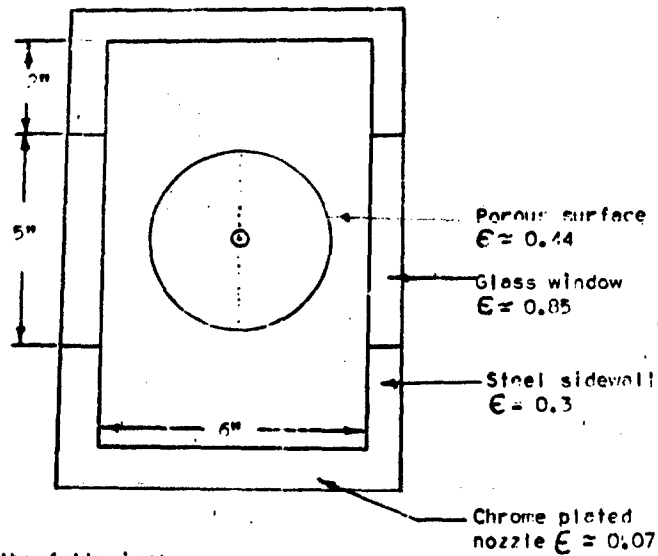
The assumptions made were the following:

a. Each element of porous surface sees chrome ($\epsilon \simeq 0.07$) over an angle of $\pi/2$ in the axial direction of the tunnel.

b. The effective emissivity may be found by averaging on a basis of weighting by angles.

c. The surrounding temperatures are equal to the measured nozzle wall temperature.

d. The portion of the total hemicylinder that has each value of emissivity is equal to $\varphi_{\epsilon_i}/\pi/2$ where φ_{ϵ_i} is the angle in the cross-sectional plane substended by each surface i of emissivity ϵ_i.

With these assumptions:

$$\epsilon_{eff} = \sum_{i=1}^{3} \frac{\varphi_{\epsilon_i}}{\frac{\pi}{2}} \epsilon_i \qquad (A\text{-}18)$$

$$(i = 1), \tfrac{1}{2}\varphi_{roof} = \tfrac{1}{2}\varphi_{0.07} = \tan^{-1}\left[\frac{3}{4.5 - r_o}\right]$$

$$(i = 2), \tfrac{1}{2}\varphi_{wall} = \tfrac{1}{2}\varphi_{0.3} = \tan^{-1}\left[\frac{3}{2.5 - r_o}\right] - \tan^{-1}\left[\frac{3}{4.5 - r_o}\right]$$

$$(i = 3), \tfrac{1}{2}\varphi_{window} = \tfrac{1}{2}\varphi_{0.85} = \frac{\pi}{2} - \tan^{-1}\left[\frac{3}{2.5 - r_o}\right]$$

$$r_o = x \sin \theta^o. \qquad (A\text{-}19)$$

19

Radiation losses to the test section walls were then computed from the expression:

$$q_{rad} = \sigma \epsilon_{w-n} (T_w^4 - T_n^4)$$ (A-20)

where

$$\frac{1}{\epsilon_{w-n}} = \frac{1}{\epsilon_w} + \frac{A_w}{A_n} \left[\frac{1}{\epsilon_{eff}} - 1 \right]$$ (A-21)

which properly applies to coaxial cylinders radiating diffusely (Reference 30). Combinations of Equations (A-19) and (A-21) gave values of ϵ_{w-n} ranging from 0.43 in the vicinity of $x = 2$-inches to 0.30 in the vicinity of $x = 13$ inches.

$$\frac{A_w}{A_n} = \frac{2\pi r_o dx}{2\pi R dx} = \frac{r_o}{R} = \frac{x \sin \theta}{R}$$ (A-22)

and R is the effective radius of the tunnel, the wetted perimeter divided by 2π. σ is the Stephan Boltzman constant, 0.173×10^{-8} BTU/hr - ft^2 - $^\circ$R^4.

The effect of the radiation correction may be observed by examining the recovery factor data shown in Figures 17 and 18. The measured recovery temperatures were corrected for radiation with the aid of the Chapman and Rubesin prediction for heat transfer coefficient. Neglecting surface heat conduction the energy balance reduces to

$$T_{ew} = T_{w_{meas}} - \left[\frac{\sigma \epsilon_{w-n}}{h_o} \left\{ (T_n)^4 - (T_w)^4 \right\} \right]$$ (A-23)

The Chapman and Rubesin[24] prediction for cone flow yields:

$$h_o = 0.2958 \sqrt{3} \frac{\kappa_\delta \sqrt{C'}}{x} \sqrt{\frac{U_\delta x}{\nu_\delta}}$$ (A-24)

Variable Wall Temperature Correction

The effects of non-uniform surface temperature upon the computed heat transfer coefficients were accounted for using the laminar constant property theory of Lighthill[27]. The measured cone surface temperature distributions were transformed to equivalent flat plate temperature distributions by means of the relation[28]

$$x_p = x_c^3 ,$$ (A-25)

20

and the temperature distribution in each case was approximately by
14 linear segments. With this assumption, the effect of non-uniform
surface temperature on local laminar heat transfer coefficient is
found by the relation

$$\frac{q}{\bar{q}}\Bigg]_{x_n} = + \frac{1}{T_w - T_w(0+)} \sum_{i=1}^{n} c_{ni}(T_{w_i} - T_{w_{i-1}}) \tag{A-26}$$

where $T_w(0+)$ is the temperature immediately downstream of the leading
edge and barred quantities refer to values for constant surface
temperatures. Also,

$$c_{ni} = \frac{x_n}{x_i - x_{i-1}} \left[G\frac{x_{i-1}}{x_n} - G\frac{x_i}{x_n} \right] \tag{A-27}$$

where $G(x)$ is presented in Reference 28.

The data reduction for all the experimental work included in
this experimental work included in this report has been programmed
and computed on a Royal McBee LGP-30 digital computer. Most of the
programming was done using "Dictator", an artificial language for
the LGP-30 programmed by C. W. Laudeman of Dodco Incorporated to
permit three-address programming and floating point operation with
a vocabulary of commands greatly increased over that available in
the basic machine language.

The data was punched on paper tape directly from the raw data
sheets, and the machine was used for sorting and tabulating functions
as well as for computing. After the original tape was punched and
proof read, all subsequent operations were machine controlled, thus
avoiding transcription errors.

APPENDIX B

SOLUTION OF THE CONSTANT INJECTION CASE

An analysis is presented which predicts the skin friction characteristics of a compressible laminar boundary layer with fluid injection.[*] The present formulation is restricted to a linear variation of fluid viscosity with temperature. For the injection cases considered, the coolant gas is considered to be identical to the main stream fluid. In the cases where similarity exists, the method is tested by comparisons with exact solutions which are free from the limitations of the present analysis.

Integral techniques generally furnish engineering accuracy for laminar skin friction and surface heat transfer calculations even when crude approximations are made in the profiles. In the present analysis the shear profile is assumed to be a third degree polynomial in velocity. This approach furnishes accuracies comparable with fifth or sixth degree polynomials in the velocity versus y/δ formulation and provides the additional benefit that the concept of boundary layer thickness (or thicknesses) does not appear in the problem.

The practical application of boundary layer analyses is the prediction of local skin friction and heat flux rates along a body from specified boundary conditions such as Mach number and altitude. The detailed structure of the interior of the boundary layer is of practical interest only through its influence on the wall conditions attained. Similarity analyses (dependent variables expressed in terms of only one independent variable) do provide general solutions to the boundary layer equations. However, the property of similarity of the characteristic profiles is possible only for certain combinations of the independent variables. For example, with injection, similarity exists only if the wall velocity varies inversely with the square root of the distance along the body. Such inverse half-power blowing distributions are only conveniently attained if the surface effusion velocity is controlled by the heat and mass transfer characteristics of the boundary layer.

With these considerations in mind it is reasonable to develop approximate methods which satisfy the boundary layer equations only on the average across the boundary layer and yet allow more general boundary conditions to be met. This situation is obtained by integrating the boundary layer equations across the boundary layer. The physical quantities appearing in the integrand are approximated by polynomials in the space variables with coefficients which are determined from the boundary conditions. With the assumption of these profiles the integral-differential equations can be converted to ordinary differential equations which describe the variation of wall skin friction along the body.

---

[*] A detailed treatment of the associated heat transfer effects is presented in Reference 26. The heat transfer calculations are too lengthy to be repeated here.

22

The use of a large number of free stream boundary conditions adds little to the accuracy of the calculated wall parameters. The reverse is true for the wall boundary conditions. The zeroeth and higher order derivatives of the boundary layer equations furnish additional restraints when evaluated at the wall. This process begins to generate difficulties when gradients along the wall first appear since an additional ordinary differential equation must now be solved simultaneously with each integral equation. This condition therefore limits the number of wall boundary conditions which may be used. The use of a finite number of terms in the profiles excludes the exact solution from consideration.

When the analysis is carried out in physical space the conditions at the outer edge are imposed at some finite distance from the wall called δ, the boundary layer thickness, which ignores the asymptotic nature of the true physical profiles. In velocity space the problem is simplified since the integration is carried from the wall to the free stream velocity; hence the range of integration is zero to one. If shear is used as a dependent variable then the free stream conditions occur at an infinite distance from the wall.

ANALYSIS

The basic equations for a compressible laminar boundary layer with no pressure gradient and for a perfect, single-component, gas with constant Prandtl number and specific heat are:

$$(\text{continuity}) \quad (\rho u)_x + (\rho v)_y = 0 \tag{B-1}$$

$$(\text{momentum}) \quad \rho u u_x + \rho v u_y = (\mu u_y)_y \tag{B-2}$$

$$(\text{energy}) \quad \rho u i_x + \rho v i_y = \frac{1}{Pr}(\mu i_y)_y + \mu(u_y)^2 . \tag{B-3}$$

In addition the fluid viscosity shall be required to take the form

$$\frac{\mu}{\mu_s} = C \frac{T}{T_s} . \tag{B-4}$$

This assumption uncouples the momentum equation from the energy equation so that the momentum equation may be independently solved. It is simplest to treat the case C = 1 in this text. In an alternate procedure the constant C is chosen so that the correct value of viscosity, as given by the Sutherland law, is evaluated at the average wall temperature.

To solve this system of equations the transformations of L. Crocco are employed. In this formulation u replaces y as one of the independent variables while the shear stress τ replaces u as one of the dependent variables. Let

23

$$\mathcal{E} = x, \qquad \bar{u} = u\,(x,y). \tag{B-5}$$

The transformation relations become

$$()_x = ()_{\mathcal{E}} - \frac{y}{y_u}\,()_u; \quad ()_y = \frac{1}{y_u}\,()_u \tag{B-6}$$

which reveal the basic difficulty in defining the outer edge of the boundary. The product ρv may be eliminated from the momentum equation through the use of the continuity equation. Applying the transformation relations (B-6) results (with $\tau = \mu u_y$) in

$$\tau^2 \tau_{uu} = \rho\mu u \tau_x. \tag{B-7}$$

It is convenient to introduce non-dimensional quantities. Let

$$\tau^* = \frac{\tau}{\rho_\delta u^2_\delta}; \quad (\tau_w^* = \frac{C_f}{2}); \quad \bar{u} = \frac{u}{u_\delta} \tag{B-8}$$

Equation (B-7) then takes the form

$$\tau^{*2}\tau^*_{uu} = \frac{\nu_\delta}{u_\delta}\,\bar{u}\tau^*_x. \tag{B-7'}$$

The appropriate extreme conditions are:

<u>Initial conditions</u>

$$x = 0, \; 0 < u < u_\delta; \quad \lim_{x \to 0}\tau^* = \infty \tag{B-9}$$

<u>Boundary conditions</u>

$$x > 0, \; \bar{u} = 0; \quad \tau^* = \tau_w^*$$
$$x > 0, \; \bar{u} = 1; \quad \tau^* = 0 \tag{B-10}$$

<u>Added restraints</u>

Other useful relations of interest may be obtained from the momentum equation (B-2) and equations resulting from it after differentiation with respect to u. For example, the momentum equation (B-2) may be written

$$\rho u u_x + \rho v \frac{\tau}{u} = \tau_y = \frac{\tau}{\mu}\tau_u \tag{B-2}$$

24

so that

$$\tau_{u_w} = \rho_w v_w(x), \quad \tau^*_{u_w} = \frac{\rho_w v_w}{\rho_\delta u_\delta}$$

Evaluating Equation (B-7') for a wall point ($\bar{u} = 0$) results in:

$$\tau_{uu_w} = 0, \quad \tau^*_{uu_w} = 0$$

$$x > 0, \quad \bar{u} = 0$$

$$\tau^*_{u_w} = \frac{\rho_w v_w}{\rho_\delta u_\delta} ; \quad \tau^*_{uu_w} = 0. \tag{B-1.}$$

Expanding τ^* in a cubic polynomial in $\bar{u}$ results in:

$$\tau^* = \tau^*_w + \left[\frac{\rho_w v_w}{\rho_\delta u_\delta}\right] \bar{u} - \left[\tau^*_w + \frac{\rho_w v_w}{\rho_\delta u_\delta}\right] \bar{u}^3 \tag{B-12}$$

The dimensionless shear profile (B-12) is introduced into the transformed momentum equation (B-7') which is then integrated from $\bar{u} = 0$ to $\bar{u} = 1$ (across the boundary layer) to yield:

$$\frac{\nu_\delta}{u_\delta}\left[\frac{7}{10}\frac{d\tau^*_w}{dx} + \frac{2}{15}\frac{d\left(\frac{\rho_w v_w}{\rho_\delta u_\delta}\right)}{dx}\right] + \left(\tau^*_w + \frac{\rho_w v_w}{\rho_\delta u_\delta}\right)\left[\frac{27}{20}\tau^{*2}_w + \frac{11}{10}\tau^*_w\left(\frac{\rho_w v_w}{\rho_\delta u_\delta}\right) + \frac{1}{4}\left(\frac{\rho_w v_w}{\rho_\delta u_\delta}\right)^2\right] = 0 \tag{B-13}$$

which must satisfy the initial conditions $x = 0$, $\lim \tau^*_w = \infty$. The extension of the shear profile to fourth degree or higher merely changes the numerical coefficient in the integrated equation (B-13) when the additional coefficients are selected at the outer edge of the boundary layer. No additional wall restraints may be added without introducing additional differential equations. Generally the injection rate is specified and the wall shear determined. Alternately the blowing rate required to produce a specified wall shear stress distribution may be computed. Numerical solutions may be easily obtained for arbitrary variations of either quantity. It is informative to first consider some special cases where analytical solutions may be obtained.

25

a.) <u>Impermeable Surface</u> $\dfrac{\rho_w v_w}{\rho_\delta u_\delta} = 0$

Equation (B-13) may be integrated directly and upon application of initial conditions (B-9) yields $C_f\sqrt{Re} = 2/3$ which compares favorably with the exact value of $C_f\sqrt{Re} = .664$ as derived by Blasius. The property values in the skin friction coefficient and the Reynolds number are all evaluated at the free stream.

It is interesting to examine the assumed velocity profiles in the physical plane. For zero injection the assumed shear profile reduces to

$$\tau^* \cdot \dfrac{\mu\frac{du}{dy}}{\rho_\delta u_\delta^2} = \tau_w^{*2}\,(1 - \bar{u}^3), \quad \dfrac{\rho_\delta u_\delta \tau_w^*(x)y}{\mu_\delta}\int_0^{\bar{u}} \dfrac{d\bar{u}}{1 - \bar{u}^3} \ . \tag{B-14}$$

For purposes of demonstration only take $\mu = \mu_\delta$ and Equation (B-14) yields upon integration from 0 to y:

$$\dfrac{y}{x}\sqrt{Re} = \ln\sqrt{\dfrac{\bar{u}^2 + \bar{u} + 1}{(\bar{u} - 1)^2}} + \sqrt{3}\,\tan^{-1}\left[\dfrac{\sqrt{3}\,\bar{u}}{\bar{u} + 2}\right] \ . \tag{B-15}$$

b.) <u>Permeable Surface with Similarity</u> $\dfrac{\rho_w v_w}{\rho_\delta u_\delta} = A\sqrt{\dfrac{\nu_\delta}{u_\delta x}}$

By taking $\dfrac{\rho_w v_w}{\rho_\delta u_\delta} = A\sqrt{\dfrac{\nu_\delta}{u_\delta x}}$ and $\tau_w^* = B\sqrt{\dfrac{\nu_\delta}{u_\delta x}}$ Equation (B-13) is found to be independent of x and yields the algebraic expression:

$$15A^3 + 81A^2 B + 147AB^2 + 81B^3 - 9B - 4A = 0 \tag{B-16}$$

Special cases of Equation (B-16) are:

1.) <u>Zero Injection</u> $(A=0), B = \sqrt{9/81} = 1/3$

2.) <u>Zero shear</u> $(B=0), A = \sqrt{4/15} = 0.516.$

As pointed out in section a, the exact value of B(A=0) as calculated by Blasius is 0.332. The exact value of A(B=0) as calculated by Emmons and Leigh[33] is 0.619. The "blow-off" injection rate is not predicted accurately by the present analysis. This large injection rate produces a boundary layer thickness so large that the boundary layer approximations resulting from the conventional order of magnitude analysis no longer provide an adequate description of the process.

26

TABLE I

Flat Plate Skin Friction and Heat Transfer Results			
$A = \dfrac{\rho_w v_w}{\rho_\delta u_\delta}\sqrt{\dfrac{u_\delta x}{\nu_\delta}}$	$\dfrac{C_f}{C_{f_0}} = \dfrac{B_A}{B_{A=0}}$	$\dfrac{C_f}{C_{f_0}}$ Emmons[33] and Leigh	$\left.\dfrac{Nu}{Nu_o}\right]_{T_w = const.}^{Pr = 0.7}$ Low[11]
0 Solid	1.000	1.000	1.000
0.1 Blowing	.798	.788	.819
0.2 Blowing	.602	.589	.643
0.3 Blowing	.410	.406	.477
0.4 Blowing	.220	.243	.322
-1 Suction	3.414	3.521	
-2 Suction	6.838	6.346	

c.) Permeable Surface With Uniform Injection $\dfrac{\rho_w v_w}{\rho_\delta u_\delta} = H$

This case considers a constant blowing rate (i.e., independent of x) so that $d(\rho_w v_w/\rho_\delta u_\delta)/dx$ is identically zero. Defining $\alpha(x) = H/u_w(x)$, Equation (B-13) reduces to:

$$\frac{5}{6} H^2 \frac{u_\delta x}{\nu_\delta} = \int_0^\alpha \frac{\alpha d\alpha}{(\alpha + 1)(\alpha^2 + \frac{22}{5}\alpha + \frac{27}{5})} . \qquad (B-17)$$

α must satisfy the initial condition $\alpha(x = 0) = 0$. The root $\alpha = -1$ corresponds to the asymptotic solution for constant suction in which the velocity distribution and all boundary layer parameters are independent of distance along the plate such that $C_f/2 = -\rho_w v_w/\rho_\delta u_\delta$. Applying Descartes' rule of signs to the denominator, the other two roots are found to be imaginary. Expanding the integrand of Equation (B-17) into partial fractions by means of the method of undermined coefficients and integrating termwise yields:

$$\frac{5}{3} H^2 \frac{u_\delta x}{\nu_\delta} = \ln\left[\frac{1}{\alpha+1}\sqrt{\frac{5\alpha^2+22\alpha+27}{27}}\right] + \frac{16}{\sqrt{14}}\tan^{-1}\left[\frac{\sqrt{14}\alpha}{11\alpha+27}\right]. \qquad (B-18)$$

It is easy to verify the requirement that the initial condition $\alpha(x=0)=0$ is satisfied. It is possible to calculate the position of blow-off since with uniform injection the condition of zero wall shear occurs somewhere on the body. The limit of the right hand side of Equation (B-18) as α approaches infinity is

$$\left(\frac{\rho_w v_w}{\rho_\delta u_\delta}\sqrt{\frac{u_\delta x}{\nu_\delta}}\right)_{\tau_w=0} = 0.579 \qquad (B-19)$$

with $\rho_w v_w / \rho_\delta u_\delta = H$. This result is comparable to the similarity injection case $(\rho_w v_w / \rho_\delta u_\delta = C/\sqrt{x})$ in which the blow-off injection rate constant was found in section b to be 0.516. In this second case the complete boundary layer is simultaneously lifted off of the plate.

d.) <u>Semi-Permeable Surface with Downstream Uniform Injection</u>

$$\frac{\rho_w v_w}{\rho_\delta u_\delta} = 0 \quad x \leq x_o$$

$$= H \quad x \geq x_o$$

The case of a solid section followed by a porous region with uniform injection rate practically applies to observation ports on high velocity vehicles or wind tunnel windows which require cooling over and above that required on the upstream surfaces. The solution is found by combining the results of sections a and d together with the requirement of a continuous surface shear stress across the interface. Equation (B-17) is integrated from $\alpha_o = H \doteq 1/3 \sqrt{u_\delta x_o / \nu_\delta}$ to α to yield:

$$\frac{5}{6} H^2 \frac{u_\delta x_o}{\nu_\delta} \left[\frac{x}{x_o} - 1 \right] = \ln \left[\frac{\alpha_o + 1}{\alpha + 1} \sqrt{\frac{5\alpha^2 + 22\alpha + 27}{5\alpha_o^2 + 22\alpha_o + 27}} \right] + \frac{16}{\sqrt{14}} \tan^{-1} \left[\frac{\sqrt{14} \, (\alpha - \alpha_o)}{5\alpha\alpha_o + 11(\alpha + \alpha_o) + 27} \right].$$

$$(B-20)$$

Equation (B-20) is plotted in Figure 30 with α_o as a parameter. The similarity injection case (Equation (B-16)) is also plotted for comparison. The blowing parameter and skin friction coefficient have been multiplied by the square root of three in order to permit comparison with conical experiments. The experimental injection rates with uniform injection are presented as solid lines with barred ends. The agreement between the present theory for uniform injection and similarity injection explains, at least on the basis of skin friction results, why the nitrogen heat transfer data presented in Figures 25 and 26 agree with the similarity theory. The agreement implies more than pure coincidence. It must be pointed out here that the experimental heat transfer data has been corrected for variable surface temperature. This procedure adds validity to a comparison of heat transfer and skin friction effects (which is, in general, a Prandtl number effect). This point is expanded further in Figure 31 which also is a purely theoretical presentation. In order to complete the reasoning, one must first compare the skin friction results with uniform injection $(x_o > 0, \rho_w v_w = \text{constant})$ with the similarity injection $(x_o = 0, \rho_w v_w = C/\sqrt{x})$. The similarity skin friction results are seen to fall slightly below the similarity heat transfer results for a Prandtl number of 0.7. On the basis of these curves, the experimental results for heat transfer with uniform injection should fall slightly

28

below the similarity heat transfer predictions. The important point to remember is that the factor $\sqrt{1-x_o/x}$ is used in the blowing parameter. Physically it is reasonable that the proper blowing parameter should vanish at the leading edge of blowing and also be relatively unaffected by the solid tip at large distances downstream.

Regarding the helium data, one cannot make firm statements regarding the solid tip and uniform injection effects. The experimental data indicates that the reasoning applied to the nitrogen data still applies. The basic question to consider is; "What phenomena altered the injection distribution from an inverse square root variation to a nearly uniform variation?". The problem is discussed further in Appendix C.

29

THE INTERRELATION OF INDUCED PRESSURE AND SURFACE INJECTION

Searching for a phenomena which is capable of altering the non-uniform blowing distribution, the question arises as to whether the viscous boundary layer-inviscid external flow interaction can no longer be neglected. Specifically we deal with the pressure interaction produced by the outward streamline deflection caused by the surface boundary layer. This phenomena is known to exist on slender bodies at hypersonic speeds and low Reyno'ds numbers. This type of pressure interaction is classified as "boundary layer induced" since the disturbance of the external flow field is due to the distribution of boundary layer displacement thickness. The result anticipated is that the induced pressure distribution modified the injected coolant distribution in the forward areas of the cone such that a more nearly constant (invariant with distance along a ray) blowing distribution results. The latter requires an induced pressure which decreases with increasing x.

The analysis which follows is adapted from Reference 34, extended to include surface mass addition. It is developed within the framework of classical boundary layer analysis in which the boundary layer is considered separately from the external flow field. Since the streamline deflection produces a new body shape, we replace the boundary and the boundary layer with an equivalent body submerged in a inviscid flow in order to estimate the inviscid flow pressure distribution. Therefore:

$$\theta = \theta_{cone} + \frac{d\delta^*}{dx} \quad , \tag{C-1}$$

where θ is the total flow deflection, θ_{cone} - the cone half-angle, and δ^* - the boundary layer displacement thickness. In Reference 34 the pressure is assumed to be a unique function $p(\theta)$ of the local total flow deflection and is expressed as a Taylor series expansion in powers of $d\delta^*/dx$ in the form

$$\frac{p}{p_{invisc}} = 1 + \frac{1}{\left(\frac{p_{invisc}}{p_\infty}\right)} \left[\frac{d\left(\frac{p}{p_\infty}\right)}{d\theta}\right]_{\theta=\theta_c} \left(\frac{d\delta^*}{dx}\right) + \ldots \tag{C-2}$$

Higher order terms may be included. These terms were found to be negligible for present purposes. The subscript "invisc" refers to a conical surface pressure in the absence of viscous effects. The inviscid cone pressure and the derivative in the square brackets were evaluated numerically from the Taylor-Maccoll solution (Reference 35).

Applying the Mangler transformation to the boundary layer solution of Emmons and Leigh for similarity injection (Reference 33),

30

$$\frac{d\delta^*}{dx} = \frac{\phi_{f_w}}{\sqrt{2}}\sqrt{\frac{\mu^*}{\rho^* u_\delta x}} \tag{C-3}$$

where ϕ_{f_w} is a parameter depending on the blowing rate f_w. The analysis presented in Appendix B was not to be used since δ^* does not appear explicitly in the analysis. The properties are evaluated at the reference enthalpy given empirically by Eckert[36] as

$$h^* = \frac{1}{2}(h_\delta + h_w) + 0.22(h_{aw} - h_\delta) \tag{C-4}$$

where
$$h_{aw} = h_\delta + \frac{1}{2}\sqrt{Pr^*}\, u_\delta^2 \quad . \tag{C-5}$$

If $h_w = h_{aw}$, Equations (C-4) and (C-5) may be combined to yield

$$\frac{h^*}{h_\delta} = 1 + 0.72\sqrt{Pr^*}\,(\gamma - 1)\,M_\delta^2 \quad . \tag{C-6}$$

If the viscosity is taken to vary linearly with temperature, Equation (C-3) may be written

$$\frac{d\delta^*}{dx} = \frac{\phi_{f_w}}{\sqrt{2}\sqrt{Re_\delta}}\left[1 + 0.72\sqrt{Pr^*}\,(\gamma - 1)\,M_\delta^2\right] \quad . \tag{C-7}$$

For $M_\delta > 1$, we may neglect the one in the square brackets and evaluate the expression for $Pr^* = 0.7$. With this assumption, Equations (C-2) and (C-7) are combined and, after numerical evaluation of the appropriate terms in Equation (C-2) ($M_\infty = 5$, $\theta_c = 8.1^\circ$), yield:

$$\frac{p}{p_{invisc}} = 1 + 0.185\,\phi_{f_w}\,\frac{M_\delta^7}{\sqrt{Re_\delta}} = 1 + 0.185\,\phi_{f_w}\,\overline{\chi} \tag{C-8}$$

where $\overline{\chi}$ is the usual hypersonic viscous interaction parameter $M_\delta^3/\sqrt{Re_\delta}$. The additional Mach number factor appears as a result of the pressure derivative in Equation (C-2). For zero injection $\phi_{f_w} = 1.73/2 - 0.87$ so the induced pressure ratio is given by

$$\left(\frac{p}{p_{invisc}}\right)_{f_w=0} = 1 + 0.16\,\overline{\chi} \quad . \tag{C-9}$$

Equation (C-8) is plotted in Figure 32 for zero injection and three cone injection rates. The induced pressure ratios are significant and have several missile design implications. A mean line through the available data on induced pressures on sharp-nosed cones as summarized by Reference 34 is also presented which tends to confirm Equation (C-9). Using the experimental values of $M_\delta = 4.33$, $R_x/in = 0.18 \times 10^6$,

31

then at $x = 1$ inch the value of $\overline{\chi}$ is 0.19. For zero injection the induced pressure ratio is found from Equation (C-9) to be 1.03 At an f_w of 1.5, the corresponding ratio is 1.09. Neither pressure increase appears capable of altering the blowing distribution although the actual ultimate effects of the external pressure variation depend on a comparison of the local external pressure and the mass flux pressure drop characteristics of the porous surface.

CORRELATION OF PERMEABILITY MEASUREMENTS ON THE POROUS CONE

In orde to insure understanding of the physical phenomena a summary of pertainent formulas, on which the permeability correlations are based, are presented here in advance of the actual data.

a. High density pipe flow

The Hagen-Poiseuille result for fully developed viscous flow in a tube is commonly written as:

$$Q = \frac{\pi r^4}{8\mu} \frac{dp}{dt} = \pi r^2 V,$$ (D-1)

where Q = volumetric rate of flow, r = tube radius, t = tube length, V = the mean velocity. Introducing the mass flux, ρV, we may write:

$$\rho V = \frac{r^2}{8\mu RT} \, p \, \frac{dp}{dt} .$$ (D-2)

Then for isothermal flow, Eq. (D-2) may be integrated over the complete path to yield:

$$\rho V = \frac{2\left(\frac{r}{4}\right)^2}{\mu RT} \left[\frac{p_u^2 - p_d^2}{2t}\right] ,$$ (D-3)

where the subscripts u and d refer to upstream and downstream positions. The term in the square brackets may be factored such that it physically represents the average pressure multiplied by the average pressure gradient

$$\left[\left(\frac{p_u + p_d}{2}\right)\left(\frac{p_u - p_d}{t}\right)\right] .$$ Despite this feature, Equation (D-3) is independent of pressure level.

b. Low density pipe flow

Hagen's derivation was repeated by Kundt and Warburg with the modification that the velocity of the gas in contact with the tube is taken as u_o instead of zero when the mean free path is comparable with the tube radius. The result of the calculation as expressed in Reference 37 is

$$\rho V = \frac{2\left(\frac{r}{4}\right)^2}{\mu RT} \left(\frac{p_u^2 - p_d^2}{2t}\right)\left[1 + \left(\frac{2}{f} - 1\right)\frac{\lambda_m}{\left[\frac{r}{4}\right]}\right]$$ (D-4)

33

where f is Maxwell's "slip flow coefficient", i.e., the fraction f of the gas molecules striking the walls of the vessel which reflect diffusely and which contribute the tangential momentum transfer to the surface. λ_m is the mean free path of the gas molecules at the mean pressure. For air at normal pressure and temperature, the value λ_m is 2.5×10^{-5} in. Inspection of Equation D-4 shows that this equation of "slip flow" is similar to the Hagen-Poiseuille result (Equation D-3) modified by a correction factor which becomes more significant as the ratio of mean free path to radius increases and as f becomes small (smooth walls). At very low pressure the second term in the square brackets dominates and the expression reduces to Knudsen's free molecular flow formula for air or orifice with $f/4 = 1$. For other values of f a correction factor must be introduced.

c. High density flow through porous media

A fluid flowing through a porous media encounters several types of resistances. One is frictional, similar to the pipe flow type, such that the pressure drop is due to the action of a shearing stress and is linear in velocity. In the second, the losses are believed to be due to the inertia of the fluid contracting and expanding through the pores. In this case the pressure gradient is proportional to the dynamic pressure of the fluid flow. On the basis of dimensional considerations, Reynolds proposed that the total flow resistance of a porous media is a linear superposition of these effects. A momentum equation may be formed as follows:

$$dp + \frac{\mu V a^2}{\left(\frac{L_1}{4}\right)} + \frac{\rho V^2 dA}{\frac{L_2}{4}} + \rho V dV = 0, \tag{D-5}$$

$$\underbrace{}_{\substack{\text{pressure} \\ \text{term}}} \quad \underbrace{}_{\substack{\text{viscous} \\ \text{term}}} \quad \underbrace{}_{\substack{\text{inertia} \\ \text{term}}} \quad \underbrace{}_{\substack{\text{momentum} \\ \text{change}}}$$

where $(L_1/4^2)$ is the viscous coefficient and $(L_2/4)$ is the inertia coefficient. Both these coefficients have dimensions of length. If isothermal flow of a perfect gas is assumed, Equation (5) may be integrated over the complete path to yield:

$$\frac{P_u^2 - P_d^2}{2} = \frac{\mu R T}{\left(\frac{L_1}{4}\right)^2} (\rho V) + \left[\frac{1}{\left(\frac{L_2}{4}\right)} + \frac{1}{2} \ln\left(\frac{P_u}{P_d}\right)\right] RT(\rho V)^2. \tag{D-6}$$

All experimental results (including the present ones) obtained to date have shown the momentum change term to be of negligible magnitude. Forming a Reynolds number as the ratio of inertial to viscous forces yields:

34

$$Re = \frac{\left(\frac{\rho V L_2}{L_2}\right)}{\frac{\rho'}{\left(\frac{L_1}{4}\right)}} = \frac{1}{4}\frac{(L_1)^2}{L_2}\left[\frac{\rho V}{\mu}\right] . \qquad (D\text{-}7)$$

The unknown length entering into the Reynolds number expression is then related directly to the ratio of the inertial and viscous resistance coefficients. The ratio of pressure forces to inertia forces may be used to define a friction factor, which, according to Equation (D-6) yields:

$$C_f = \frac{\frac{p_u{}^2 - p_d{}^2}{2t}}{\frac{1}{(L_1/4)}RT(\rho V)^2} = \frac{1}{Re} + 1 \qquad (D\text{-}8)$$

Where the term $(1/Re)$ applies to the viscous regime and the unit factor applies to the inertial regime.

Historically, studies of fluid flow through porous media have presented correlations of permeability data by means of a single, geometrically measurable dimension taken as characteristic of the porous material. This approach is valid only within a specific flow regime. The presentation in Equations (D-7) and (D-8) require two characteristic length parameters. Experimental determinations of these two parameters require an extended range of flow rates, i.e., a maximum to minimum ratio of 10^4 to 10^2, encompassing both regimes. Since the present investigation covers only the viscous regime, a single-parameter correlation should be adequate.

d. Low density flow through porous media

Neglecting both the inertial and momentum change terms, Equation (D-6) reduces to

$$\rho V = \frac{(L_1/4)^2}{\mu RT}\left[\frac{p_u{}^2 - p_d{}^2}{2t}\right] . \qquad (D\text{-}9)$$

No analytical extension of this expression to include slip effects exists. A comparison of Equations (D-3), (D-4) and (D-9) reveals the basic similarity of the structure of these equations. By analogy, we may write the following equation for low density flow through a porous media (with $L_1 = 2\sigma$):

$$\rho V = \frac{(L_1/4)^2}{\mu RT}\left(\frac{p_u{}^2 - p_d{}^2}{2t}\right)\left[1 + \left(\frac{2}{f} - 1\right)\frac{\lambda_m}{\frac{1}{4}\left[\frac{L_1}{4}\right]}\right] . \qquad (D\text{-}10)$$

This expression may be considered as a one term Taylor series expansion of Equation (D-9) in terms of the Knudsen number λ_m/L_1.

35

MODEL PERMEABILITY CALIBRATION AT LOW PRESSURES

The 16° porous cone was mounted in an available calibration chamber as shown in Figure 33. The chamber was connected to a vacuum pump - the chamber pressure was controlled by means of a gate valve. The model mass flow was controlled by means of the same sonic orifice as used in the heat transfer and transition studies. Air was used as the calibration fluid. The basic data taken were total injected mass flow, model internal pressure (p_i) and model external pressure (chamber pressure p_d). The experimental method used consisted of varying the injected mass flow while holding the chamber pressure constant. Chamber pressures of 1, 1.5, 2, 4, 8, 15, 30 and 72 centimeters of mercury absolute were studied in order to vary the average density of the injected fluid. For reference, the cone surface pressure (p_δ or p_d) as calculated from the Taylor-Maccoll theory was 0.48 cm. Hga during the wind tunnel heat transfer studies. The mean free path at this pressure at normal temperature is approximately 3.8×10^{-4} inch. Figure 34 shows a photomicrograph of the porous cone surface. The average roughness height as measured by a Brush surface profilometer with a 500 microinch radius stylus was 60 microinches (0.6×10^{-4} in). The discrepancy between this length and the pore size observed in Figure 34 (approximately 1 to 3×10^{-3} in) implies that the instrument stylus size is not correctly matched to the roughness being measured.

The results of the permeability calibration are plotted in Figures 35 and 36. The effect of slip is apparent in view of the departure of the data from the solid-line continuum theory which has a slope of unity. The permeability distribution conditions of Figure 14 are indicated by a cross symbol. With a downstream pressure of 0.48 cm. Hga. the model internal pressure varies from 0.58 cm. Hga. to 5.24 cm. Hga. This means that the pressure drop varied from 20 percent to 1000 percent of the inviscid static pressure. Induced pressures (see Appendix C) 3 to 9 percent higher would not alter the blowing distribution for either the maximum or the minimum injection rates so that induced pressure effects were eliminated as a source of injected mass flux re-orientation.

Using the atmospheric data, the viscous resistance coefficient length L, was calculated to be 1.1×10^{-4} in. which yields an effective tube radius of 0.78×10^{-4} in. Assuming a reflection coefficient of unity, the second term in the square brackets in Equation (D-10) varies from 0.128 at an average pressure of atmospheric to 17.2 at an average pressure of 0.53 cm. Hga. (the lowest wind tunnel test injection rate) and 3.2 at an average pressure of 2.86 cm Hga. (the highest wind tunnel test injection rate). This means that the permeability distribution measurements were taken under continuum conditions while the wind tunnel experiments were performed in the "slip flow" or "molecular effusion" range.

The porous core was designed, manufactured, and the atmospheric
calibration proved that the injected mass flux distribution varies as
$x^{-1/2}$. Equation (D-10) then requires L_i^2 vary as $x^{-1/2}$. During the
actual test runs the second term in Equation (D-10) is dominant so that
that pV varied as L_i or $x^{-1/4}$.

The success of Equation (D-10) in correlating the permeability
data is demonstrated in Figure 36. The deviation of the data from
the theoretical slope of unity at very low pressures (in the molecular
flow regime the collisions between the molecules are rare as compared
with the frequency of collisions with the walls) is partially due to the
finite thickness of the porous surface (non-orifice effects) as
calculated in Reference 37.

The last question to be considered concerns the effect of "slip"
on the thermal heat exchange between the injected fluid and the porous
wall. An assumption was made in the data reduction procedure that
the temperature of the injected fluid equalled that of the porous
wall at the point of emergence. No experimental evidence was gathered
on this feature. One must adopt a rather circulatory argument here
by relying on the agreement between the lowest injection rate heat
transfer data and the Chapman and Rubesin theory. This agreement
infers that the assumption stated above is valid for all injection
rates since the lowest generates the maximum "slip" effect.

REFERENCES

1. Domich, E. G., Jantscher, H. N. and Olson, D. N., Aeronautical Research Facilities, University of Minnesota, Rosemount Aeronautical Laboratories Research Report No. 152, September 1958.

2. UMRAL Staff, Proceedings of Sixth Technical Conference of the Rosemount Aeronautical Laboratories, University of Minnesota, Rosemount Aeronautical Laboratories Research Report No. 165, October 1959.

3. Scott, C. J. and Anderson, G. E., Boundary Layer Transition with Gas Injection, University of Minnesota, Rosemount Aeronautical Laboratories Research Report No. 151, July 1958.

4. Leadon, B. N., Scott, C. J. and Anderson, G. E., Mass Transfer Cooling of a 20° Porous Cone at $M = 5$, University of Minnesota, Rosemount Aeronautical Laboratories Research Report No. 143, July 1957.

5. Mickley, H. S., Ross, R. C., Squyers, A. L. and Stewart, W. E., Heat, Mass, and Momentum Transfer for Flow Over a Flat Plate with Blowing or Suction, NACA TN 3208, July 1954.

6. Tollmien, W., Ein Allgemeines Kriterium der Instabilität Laminarer Geschwindigkeitsverteilungen, Nachr. d. Ges. d. Wiss. zu Göttingen, Math.-Phys. Kl., Neve Folge, Bd. 1, Nr. 5, 1935 (NACA TM 792, 1930).

7. Schlichting, H., Zur Entstehung der Turbulenz bei Plattenströmung, Nach. Ges. Wiss. Göttingen, Math. Physik. Klasse, 181, 1933; Amplitudenverteilung und Energie Bilanz der Kleinen Störungen bei der Plattenströmung, Nach. Ges. Wiss. Göttingen, Math. Physik. Klasse, Vol. 1, 1935.

8. Lees, L. and Lin, C. C., Investigation of the Stability of the Laminar Boundary Layer in a Compressible Fluid, NACA TN 1115, 1946.

9. Dunn, D. W. and Lin, C. C., The Stability of the Laminar Boundary Layer in a Compressible Fluid for the Case of Three-Dimensional Disturbances, J. Ae. S., Vol. 19, No. 7, July 1952.

10. Libby, P. A., Kaufman, L. and Harrington, R. P., An Experimental Investigation of the Isothermal Boundary Layer on a Porous Flat Plate, J. Ae. S., Vol. 19, No. 2, February 1952.

11. Low, G. M., The Compressible Boundary Layer with Fluid Injection, NACA TN 3404, March 1955.

12. Shen, S. F. and Persh, J., The Limiting Wall Temperature Ratios Required for Complete Stabilization of Laminar Boundary Layers with Blowing, J. Ae. S., Vol. 23, No. 3, March 1956.

13. Morduchow, M., Grape, R. G. and Shaw, R. P., Stability of Laminar Boundary Layer Near a Stagnation Point of an Impermeable Wall and a Wall Cooled by Normal Fluid Injection, NACA TN 4037, August 1957.

14. Dunn, D. W. and Lin, C. C., On the Stability of Laminar Layers in a Compressible Fluid, J. Ae. S., Vol. 22, No. 7, July 1955.

38

15. Baron, J. R., *The Binary-Mixture Boundary Layer Associated with Mass Transfer Cooling at High Speeds*, M.I.T. Naval Supersonic Laboratory TR 160, May 1956.

16. Covert, E. E., *The Stability of Binary Boundary Layers*, M.I.T. Naval Supersonic Laboratory TR 217, June 1957.

17. van Driest, E. R., *Calculation of the Stability of the Laminar Boundary Layer in a Compressible Fluid on a Flat Plate with Heat Transfer.* J. Ae. S., Vol. 19, No. 12, December 1952.

18. Chapman, D. R., Kuehn, D. M. and Larson, H. K., *Investigation of Separated Flows in Supersonic and Subsonic Streams with Emphasis on The Effect of Transition*, NACA TN 3869, March 1957.

19. Pappas, C. C. and Okuno, A. F., *Measurements of Skin Friction of the Compressible Turbulent Boundary Layer on a Cone With Foreign Gas Injection*, J. Aero/Space Sciences, Vol. 27, No. 5, May 1960.

20. van Driest, E. R. and Boison, J. C., *Experiments on Boundary Layer Transition at Supersonic Speeds*, J. Ae. S., Vol. 24, No. 12, December 1957.

21. Jack, J. P., Wisniewski, R. J. and Diaconis, N. S., *Effects of Extreme Surface Cooling on Boundary Layer Transition*, NACA TN 4049, October 1957.

22. van Driest, E. R. and McCauley, W. D., *The Effect of Controlled Three-Dimensional Roughness on Boundary Layer Transition at Supersonic Speeds*, J. Aero/Space Sciences, Vol. 27, No. 4, April 1960.

23. Leadon, B. M., *Some Experimental Techniques in Mass Transfer Cooling*, Aero/Space Engineering, Vol. 18, No. 10, October 1959.

24. Chapman, D. R. and Rubesin, M. W., *Temperature and Velocity Profiles in the Compressible Laminar Boundary Layer with Arbitrary Distribution of Surface Temperature*, J. Ae. S., Vol. 16, No. 9, September 1949.

25. Scott, C. J., *The Mangler Transformation as Applied to Porous Cones and Hemispheres*, University of Minnesota, Rosemount Aeronautical Laboratories EM 68, September 1956.

26. Scott, C. J., *Integral Laminar Boundary Layer Solutions Using the Crocco Variables*, University of Minnesota, Rosemount Aeronautical Laboratories EM 86, August 1959.

27. Lighthill, M. J., *Contributions to the Theory of Heat Transfer Through a Laminar Boundary Layer*, Proceedings of the Royal Society of London, Series A, Vol. 202, 1950.

28. DeCoursin, D. G., Sheppard, J. J. and Bradfield, W. S., *Calculation Methods for Determining the Effect of Nonuniform Surface Temperatures on Heat Transfer Through Laminar Boundary Layers on Plates and Cones*, University of Minnesota, Rosemount Aeronautical Laboratories EM 60, October 1955.

29. Woodside, W., Calculation of the Thermal Conductivity of Porous Media, Canadian Journal of Physics, Vol. 36:2, No. 7, July 1958.

30. Eckert, E. R. G., Introduction to the Transfer of Heat and Mass, McGraw-Hill Book Co., Inc., 1950.

31. Forscheimer, P., Wasserbewegung durch Boden; zeitschrift des Verlines deutscher Ingeieure 45:1701, 1901.

32. Hill, J. A. F., The Permeability of Porous Walls, M.I.T. Naval Supersonic Laboratory WTP-TM-4, September 1956.

33. Emmons, H. W. and Leigh, D. C., Tabulation of the Blasius Function with Blowing and Suction, British Aeronautical Research Council TR-CP-157, 1954.

34. Hayes, W. D. and Probstein, R. F., Hypersonic Flow Theory, Academic Press, New York, 1959.

35. Taylor, G. I. and Maccoll, J. W., The Air Pressure on a Cone Moving at High Speed, Proc. Roy. Soc. London, Ser. A., 1933.

36. Eckert, E. R. G., Engineering Relations for Friction and Heat Transfer to Surfaces at High Velocity Flow, J. Ae. S., Vol. 22, 1955.

37. Brown, G.P., DiNardo, A., Cheng, G. K. and Sherwood, T. K., The Flow of Gases in Pipes at Low Pressures, Journal of Applied Physics, October 1945.
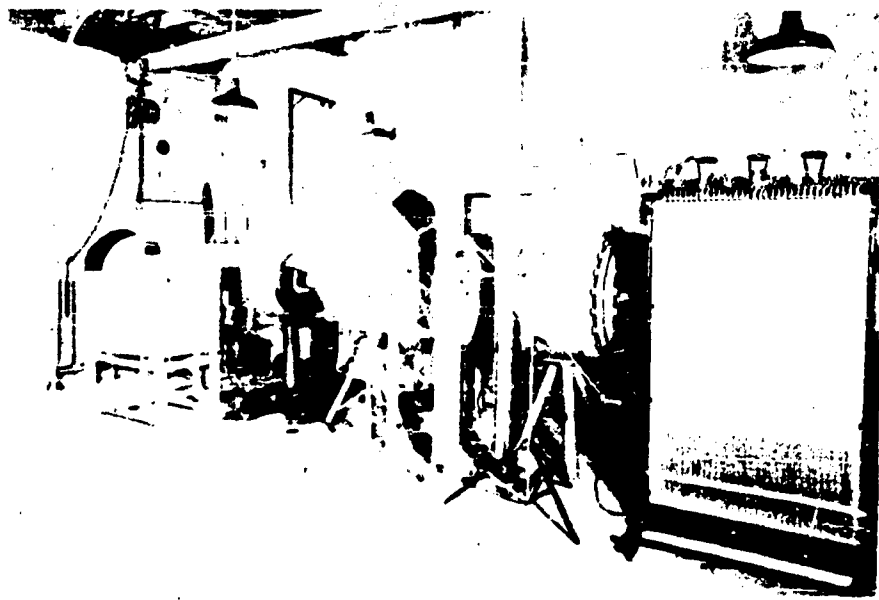
FIGURE 1. THE CONTINUOUS SUPERSONIC WIND TUNNEL.
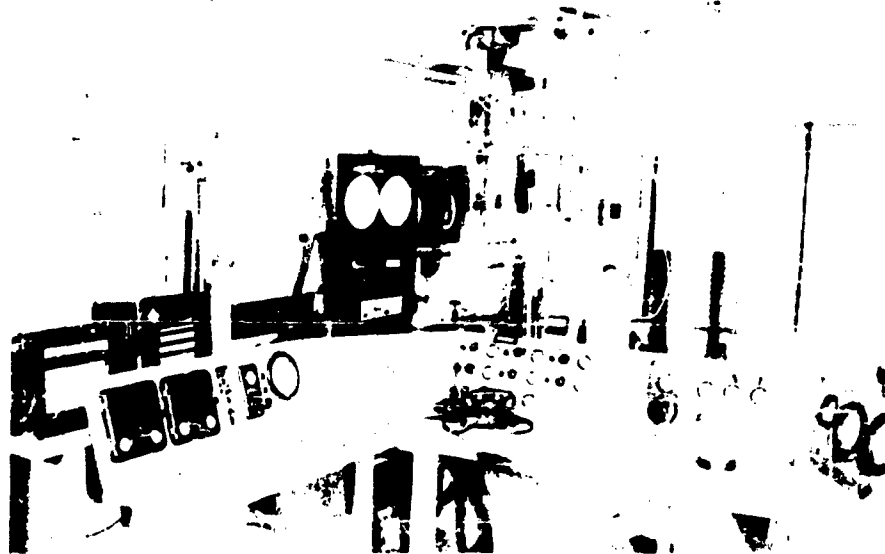
FIGURE 2. INSTRUMENTATION AND CONTROL ROOM FOR THE CONTINUOUS SUPERSONIC WIND TUNNEL.
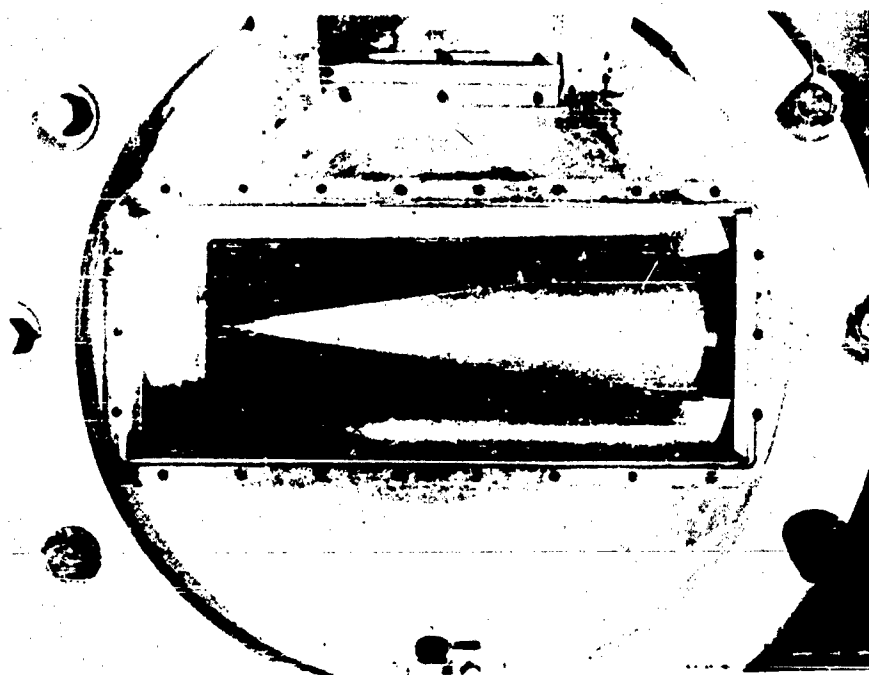
FIGURE 3.   PHOTOGRAPH OF THE 16° POROUS CONE INSTALLED IN THE
MACH 5 CONTINUOUS SUPERSONIC WIND TUNNEL.
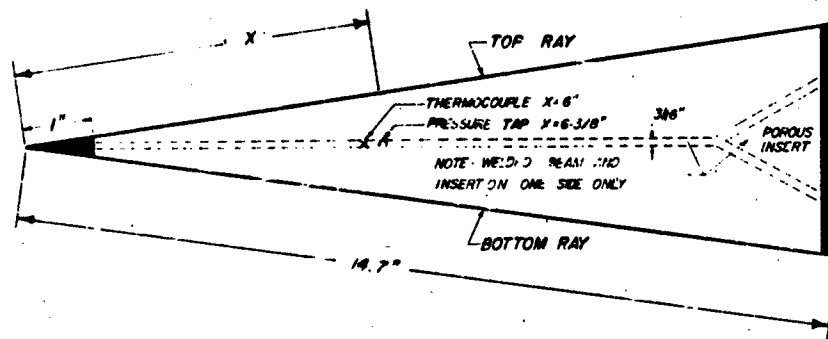
FIGURE 4.   LINE DRAWING OF TRANSITION MODEL SHOWING THE
INSTRUMENTATION POSITIONS, WELDED SEAM AND POROUS INSERT.

FIGURE 5   SHADOWGRAPH PHOTOGRAPHS: (a) NO INJECTION, (b) HELIUM AT 0.8 X THEORETICAL BLOWOFF, (c) HELIUM INJECTION AT 12 X THEORETICAL BLOWOFF, AND (D) HELIUM INJECTION AT 16 X THEORETICAL BLOWOFF.
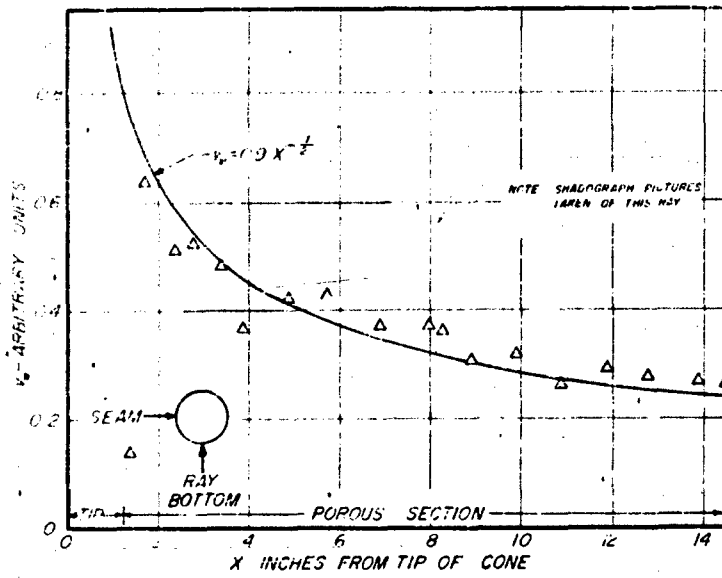
FIGURE 6A CALIBRATION OF THE INJECTED MASS FLUX DISTRIBUTION
ALONG THE SURFACE OF THE TRANSITION POROUS CONE.
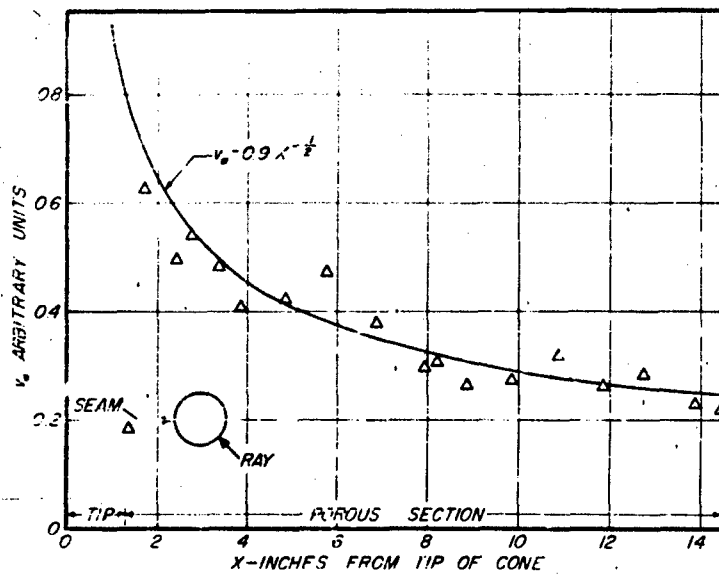
FIGURE 6B

FIGURE 5c

FIGURE 5

NOTE SHADOGRAPH PICTURES TAKEN IF THIS RAY

TOP

POROUS SECTION

x — INCHES FROM TIP OF CONE

FIGURE 6b

NITROGEN
$R_x/inch = .364 \times 10^6$
$\Delta T_w/T_0 = .05$

R_{x_t} MILLIONS

f_W
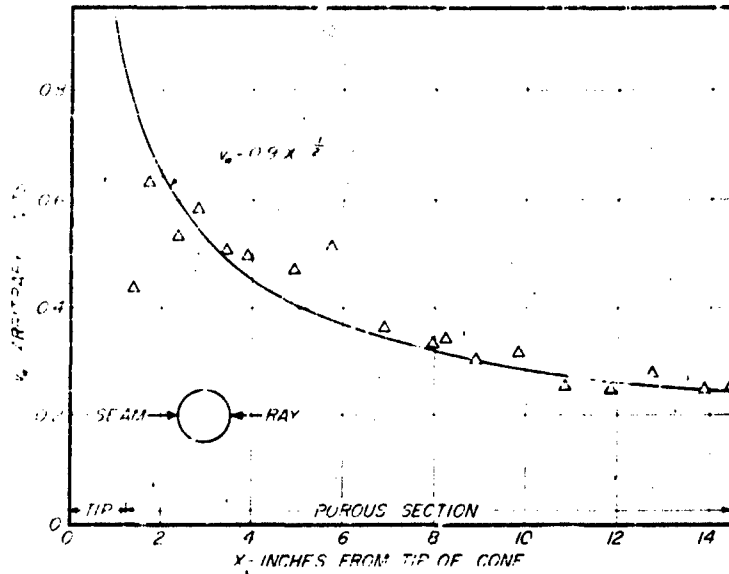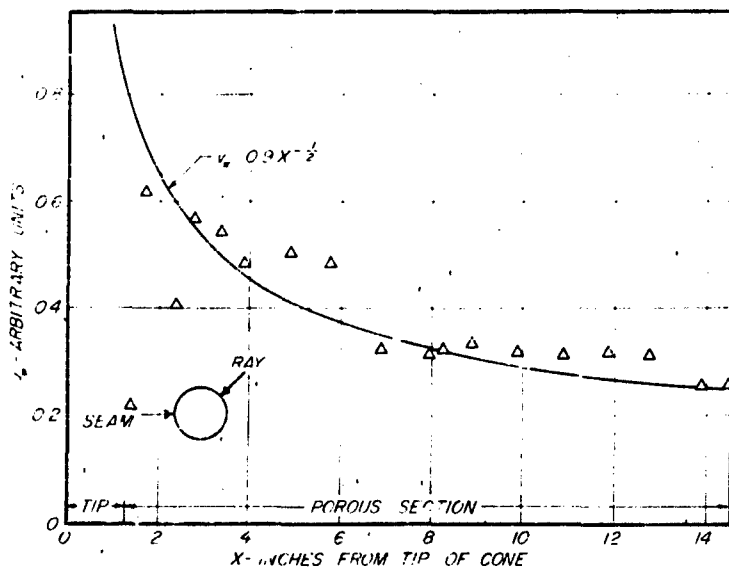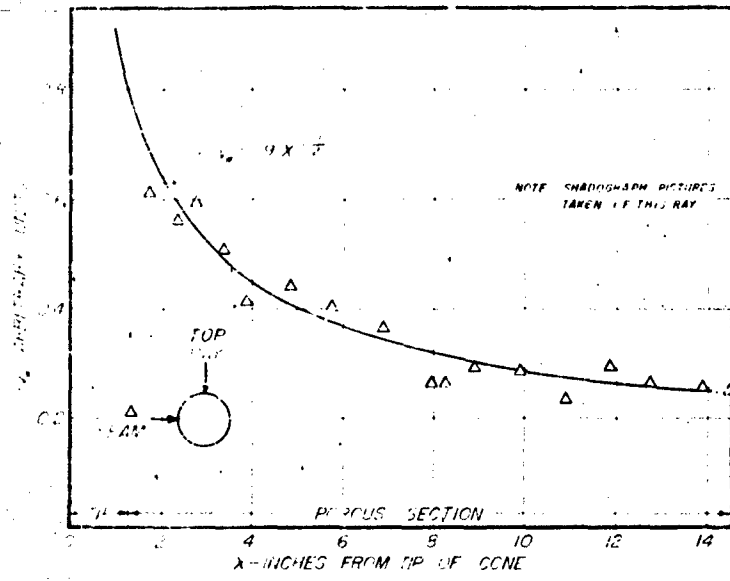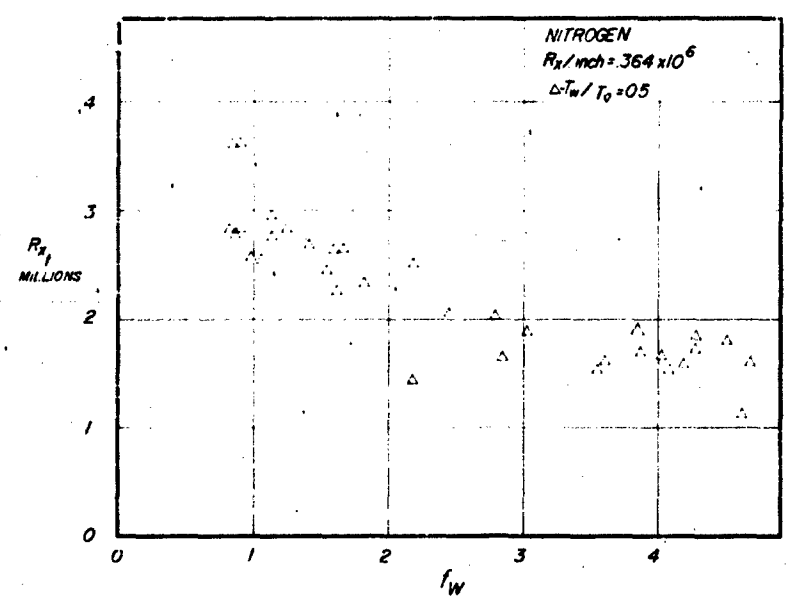
FIGURE 7a   THE REDUCTION OF TRANSITION REYNOLDS NUMBER WITH NITROGEN INJECTION.

NITROGEN
$R_x/inch = .364 \times 10^6$
△ $T_w/T_o = 0.65$

FIGURE 7a

NITROGEN
$R_x/inch = .364 \times 10^6$
△ $T_w/T_o = 0.8$
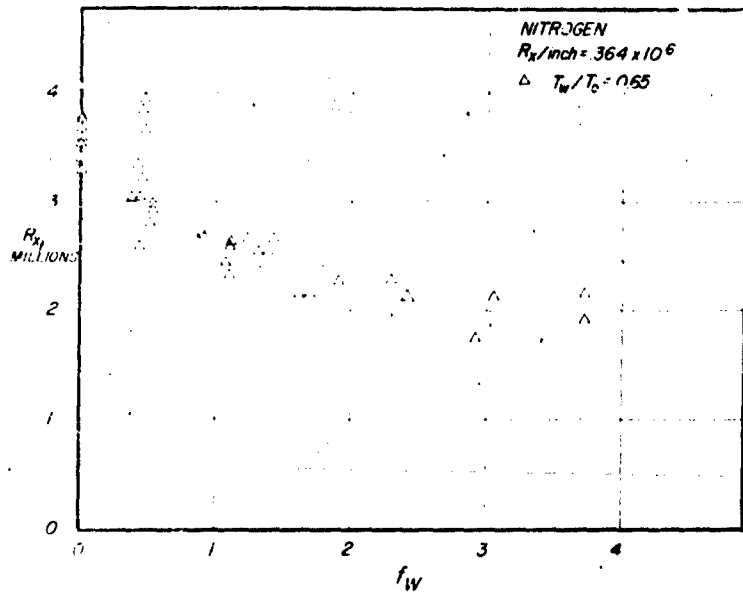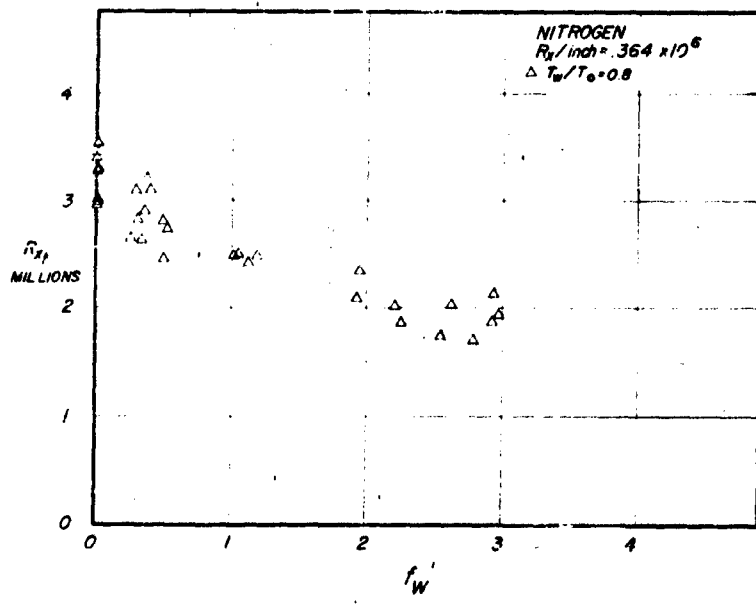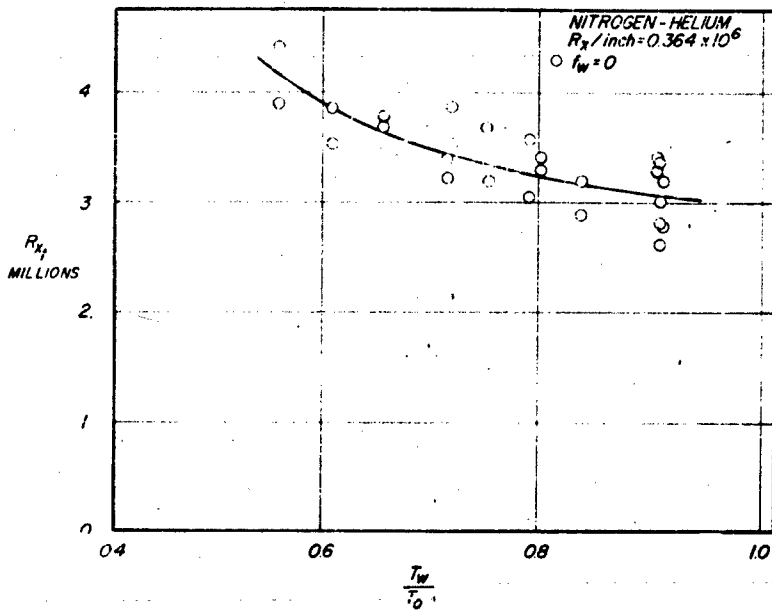
FIGURE 7c

FIGURE 8a   THE VARIATION OF TRANSITION REYNOLDS NUMBER WITH
SURFACE HEAT TRANSFER - NITROGEN INJECTION.

FIGURE 8b

FIGURE 8c

FIGURE 8d

NITROGEN
$R_x/inch = 0.364 \times 10^6$
$\triangle\ t_w' = 2.0$

R_{x_1} MILLIONS

$\frac{T_W}{T_0}$

FIGURE

NITROGEN
$R_x/inch = 0.364 \times 10^6$
$\triangle\ t_w' = 3.0$

R_{x_1} MILLIONS

$\frac{T_W}{T_0}$
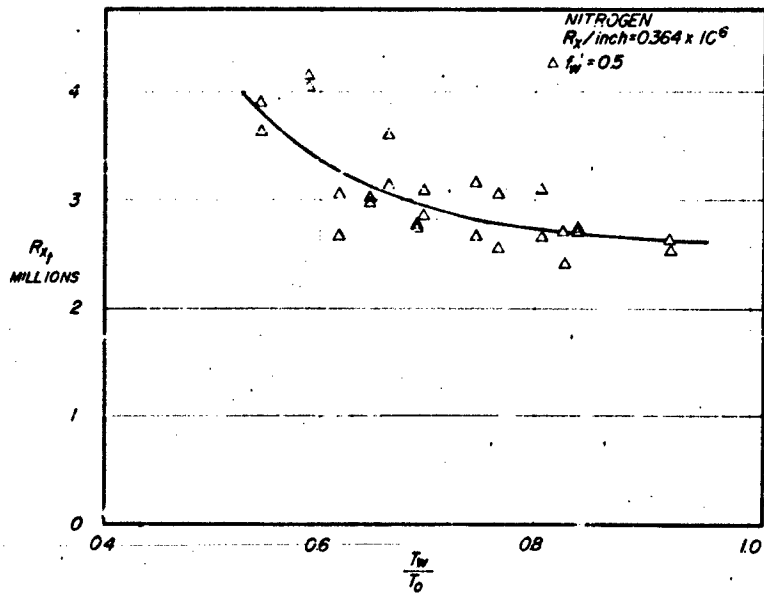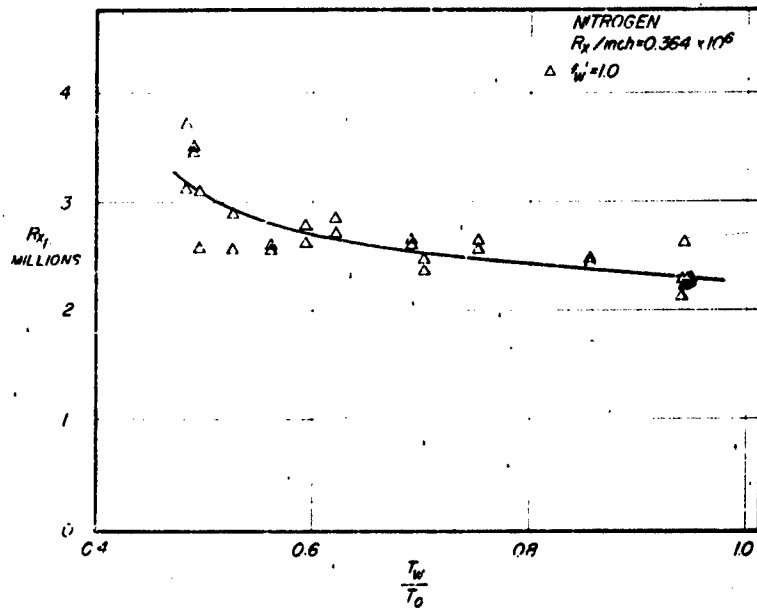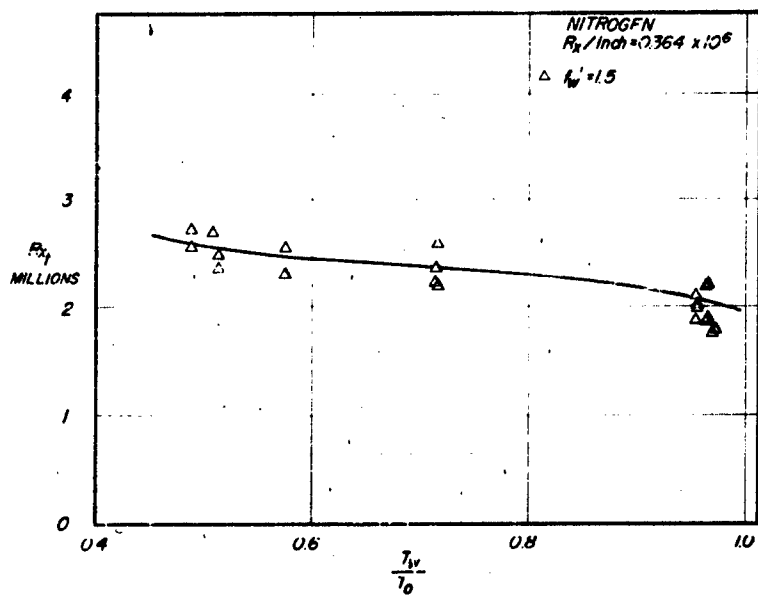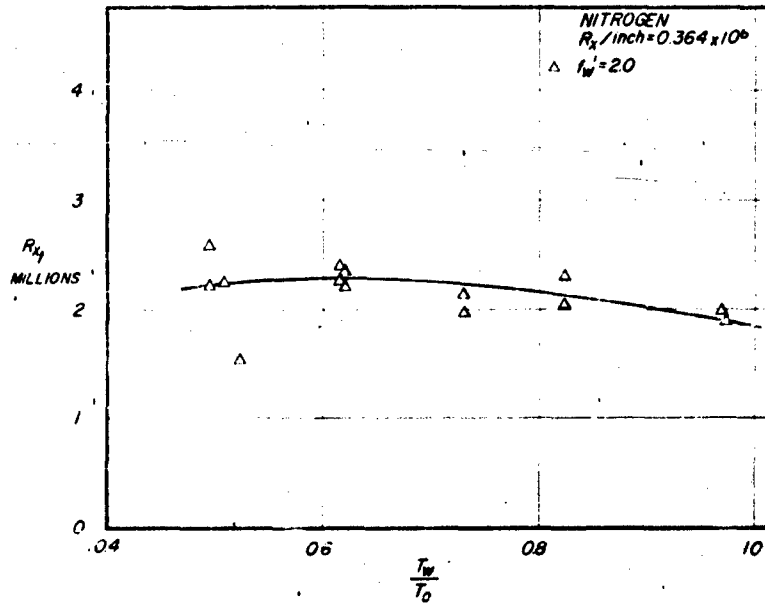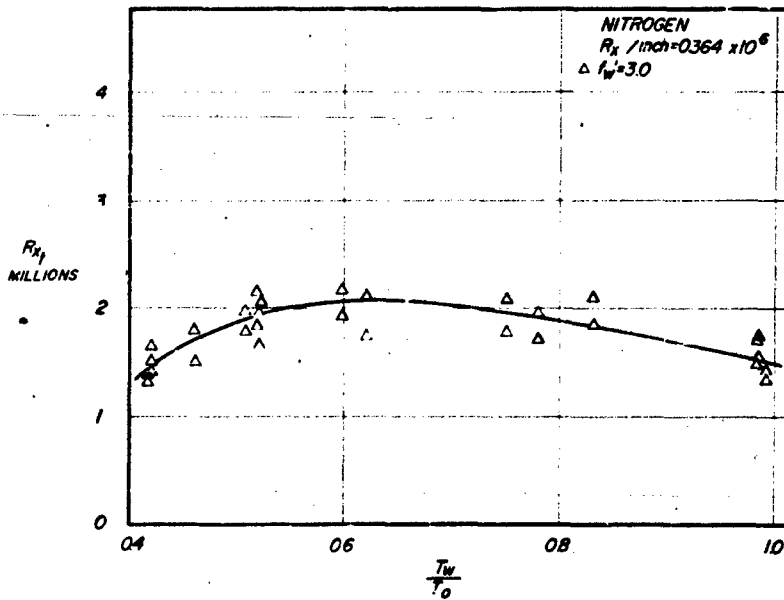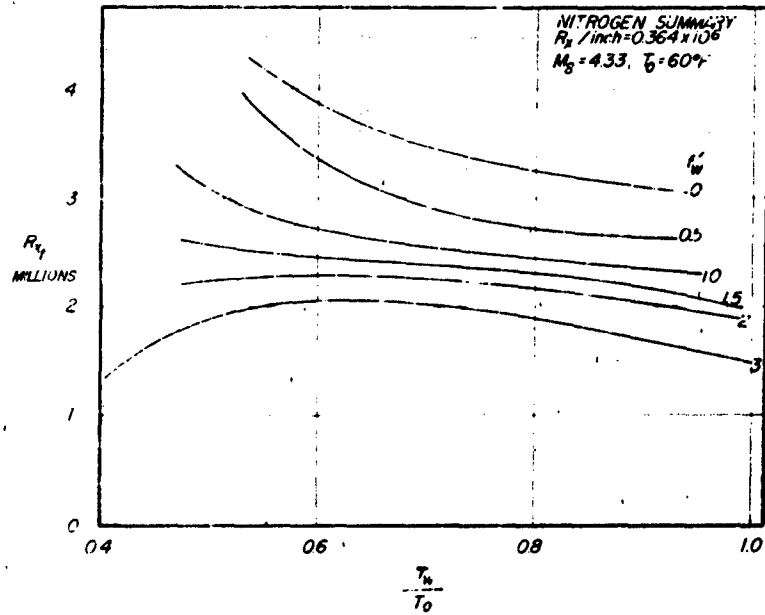
FIGURE

FIGURE 9. A SUMMARY OF THE TRANSITION RESULTS WITH
NITROGEN INJECTION.
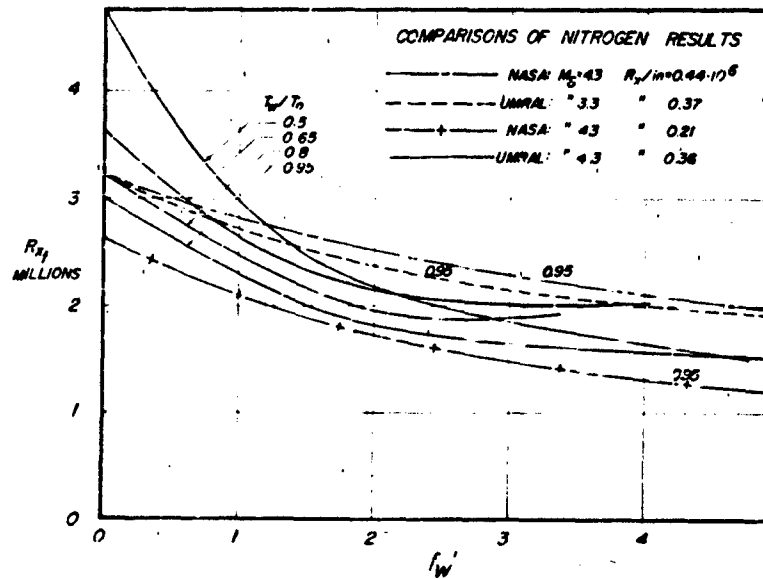
FIGURE 10. A COMPARISON OF THE PRESENT TRANSITION RESULTS
WITH OTHER EXPERIMENTAL DATA - NITROGEN INJECTION.
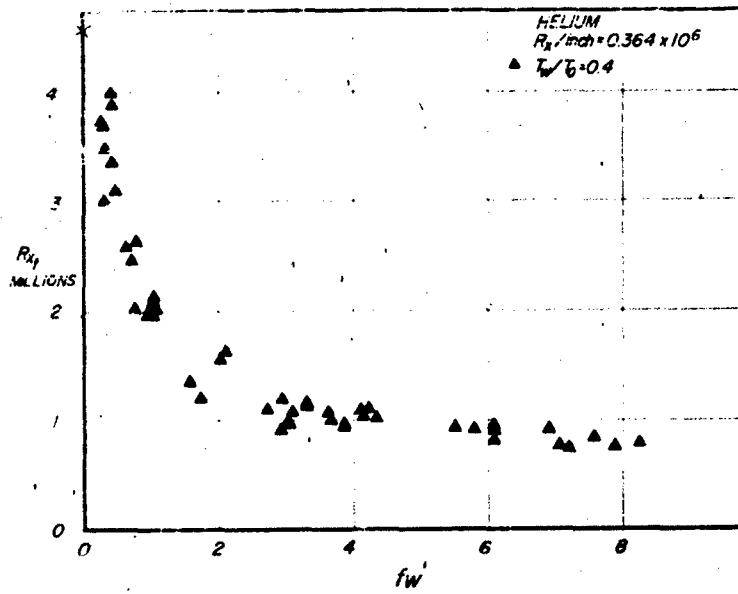
FIGURE 11a   THE REDUCTION OF TRANSITION REYNOLDS NUMBER WITH HELIUM
INJECTION.
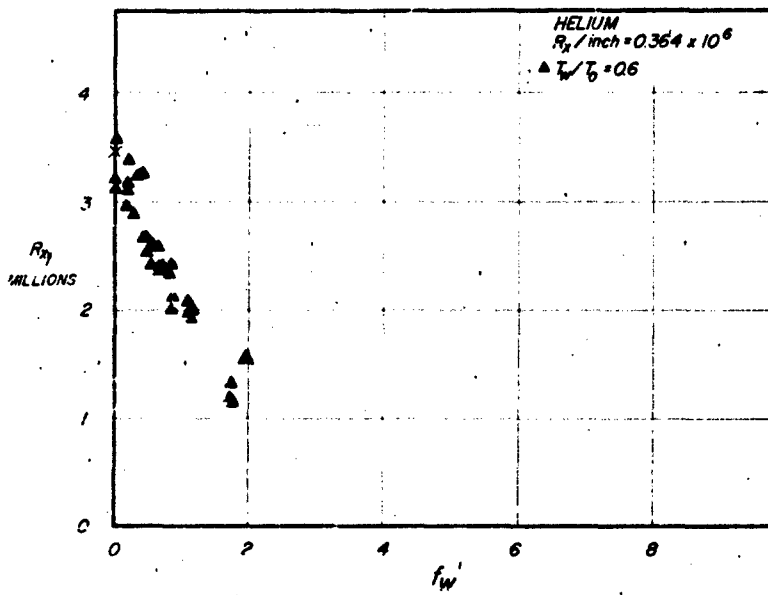
FIGURE 11b
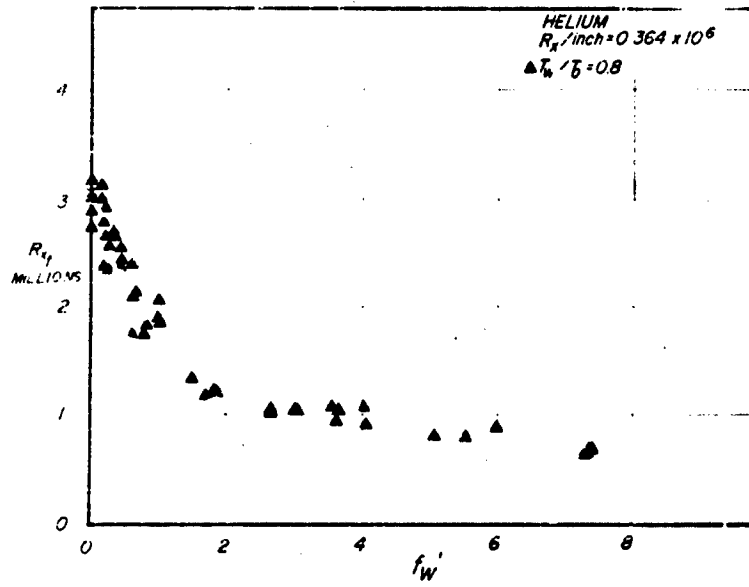
FIGURE 11a
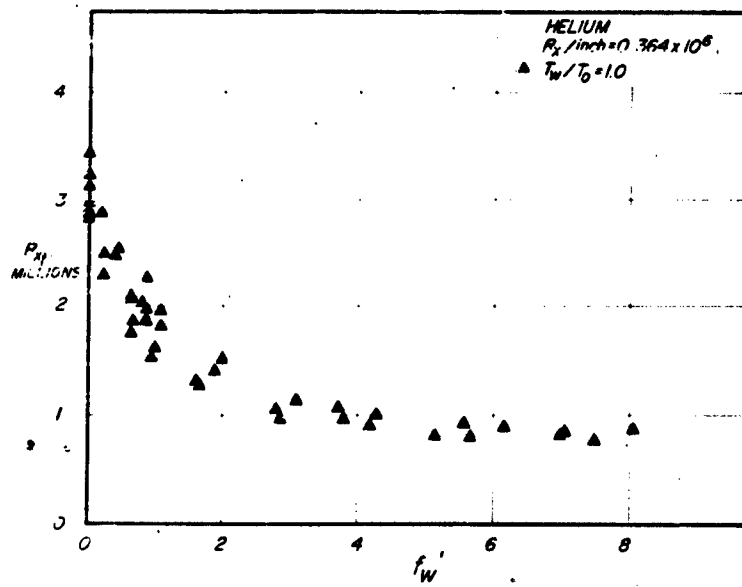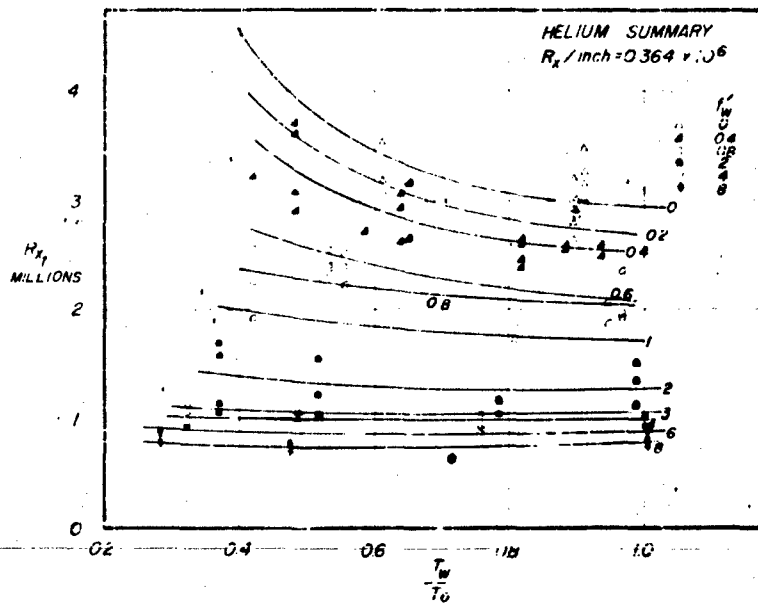
FIGURE 11b

FIGURE 12. A SUMMARY OF THE TRANSITION RESULTS WITH HELIUM INJECTION.
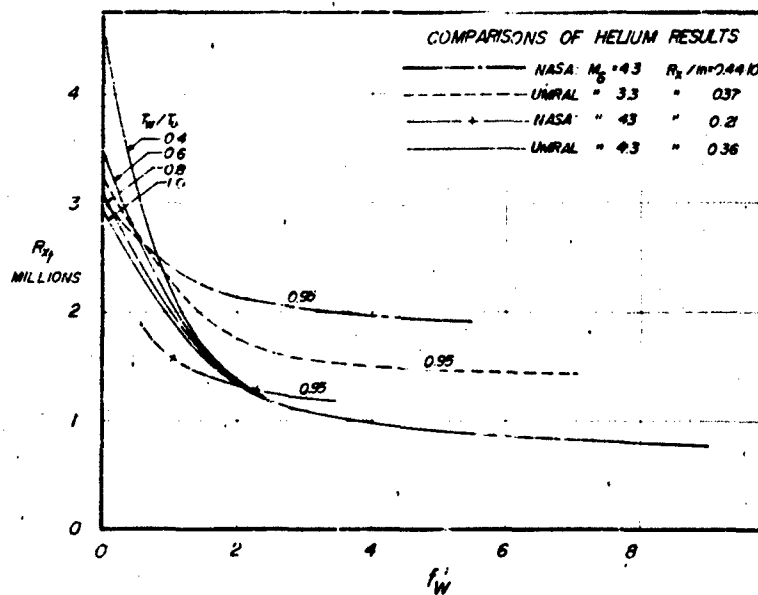
FIGURE 13. A COMPARISON OF THE PRESENT TRANSITION RESULTS WITH OTHER
EXPERIMENTAL DATA - HELIUM INJECTION.

WINDOW

SURFACE
THERMOCOUPLES

BULKHEAD — AFTERBODY

COOLANT STAGNATION
TEMPERATURE AND
PRESSURE

INTERIOR
THERMOCOUPLES

O-RING FLANGE

THERMOCOUPLE
OUTLET TUBE

SOLID TIP

FOAM

STING

VACUUM JACKET

THERMOCOUPLE
GUIDE TUBE

GAS
INLET
TUBE

ORIFICE

MODEL SUPPORT
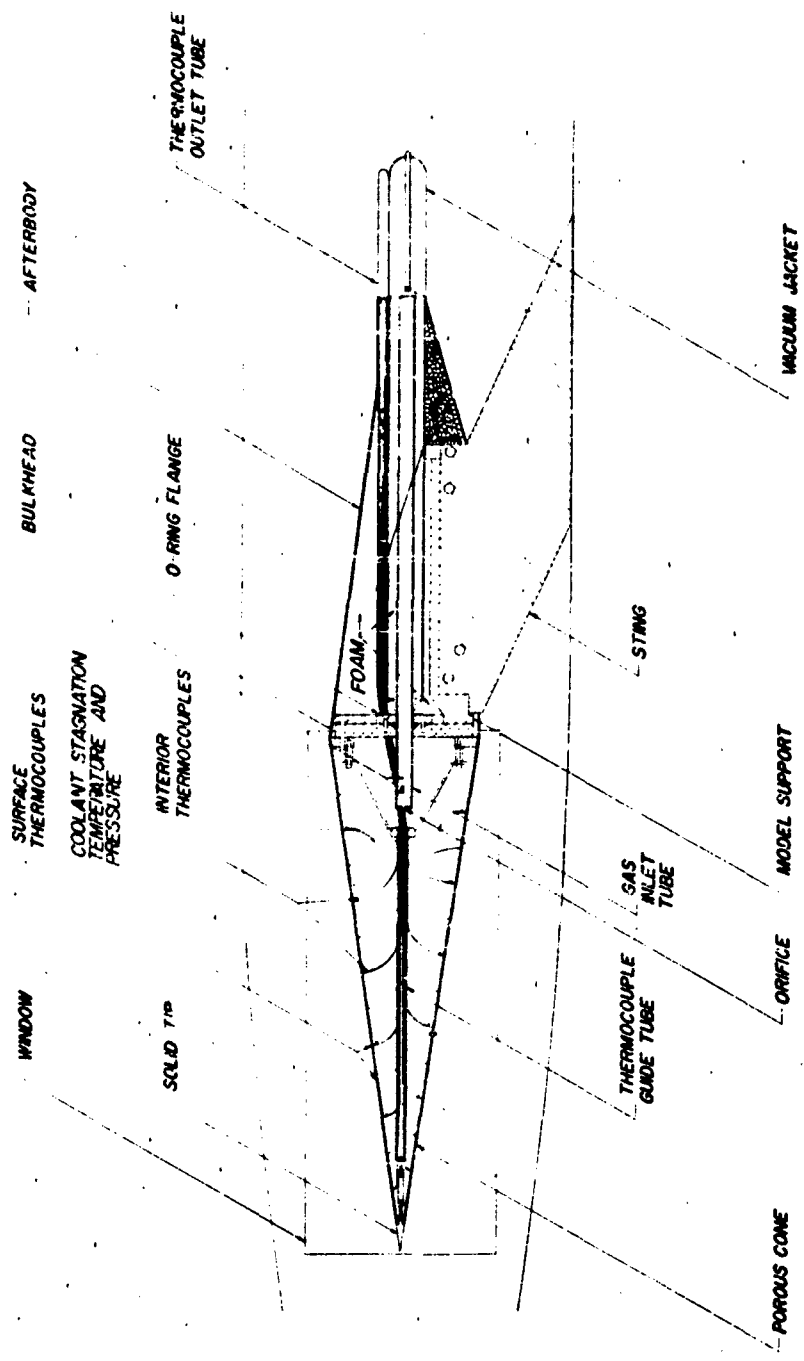
POROUS CONE

FIGURE 14. LINE DRAWING OF THE 16° POROUS CONE HEAT TRANSFER MODEL.

Legend (right side):
- VACUUM LINE
- NEEDLE VALVE
- CALIBRATED TUBE
- SOAP SOLUTION
- OPEN BELL
- MANIPULATOR
- SURFACE PROBE
- POROUS CONE
- METERING ORIFICE
- PRESSURE GAGE
- REGULATOR
- VALVE
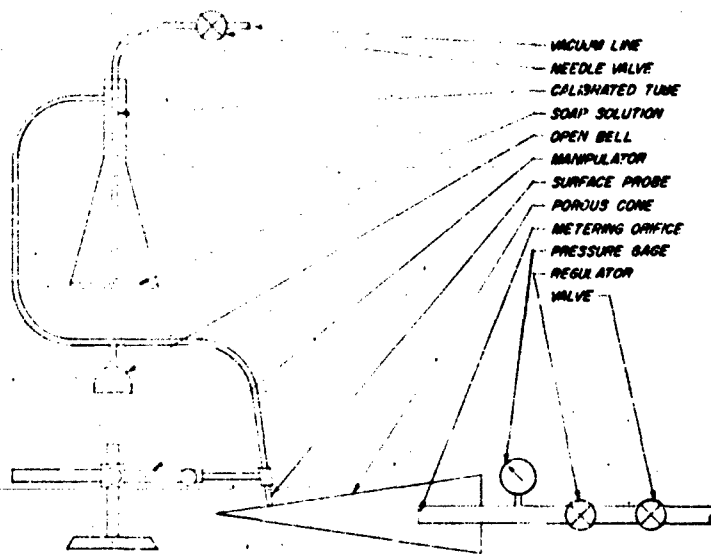
FIGURE 15. EXPERIMENTAL CALIBRATION SETUP FOR PERMEABILITY
DISTRIBUTION STUDIES ON POROUS HEAT TRANSFER MODEL
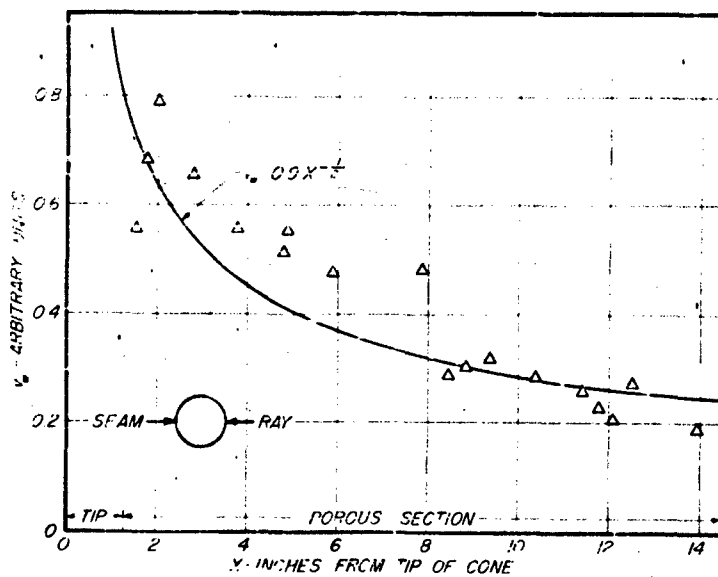
FIGURE 15A. CALIBRATION OF THE INJECTED MASS FLUX DISTRIBUTION ALONG
THE SURFACE OF THE POROUS HEAT TRANSFER CONE.

$v_o = 0.9 X^{-\frac{1}{2}}$

RAY

SEAM →

TIP ←→ ——POROUS SECTION——

X-INCHES FROM TIP OF CONE

FIGURE 16a

$v_o = 0.9 X^{-\frac{1}{2}}$

NOTE SHADOGRAPH PICTURES
TAKEN OF THIS RAY

TOP
RAY

—SEAM →

TIP ←← ——POROUS SECTION——

X-INCHES FROM TIP OF CONE
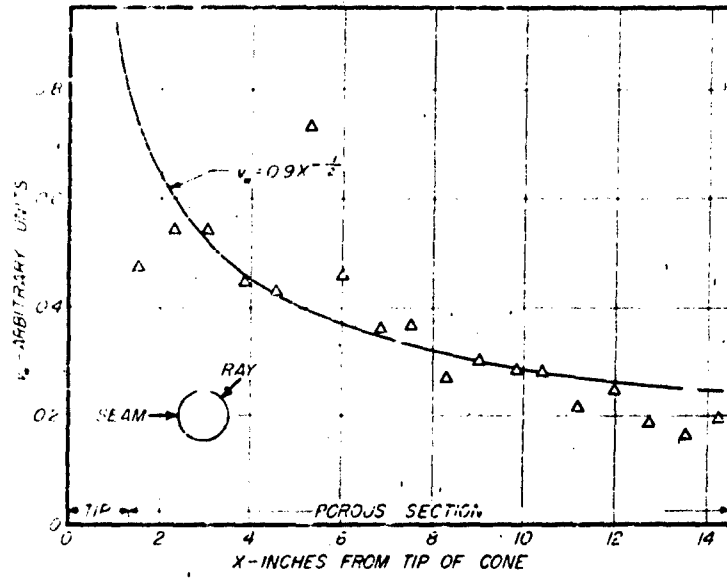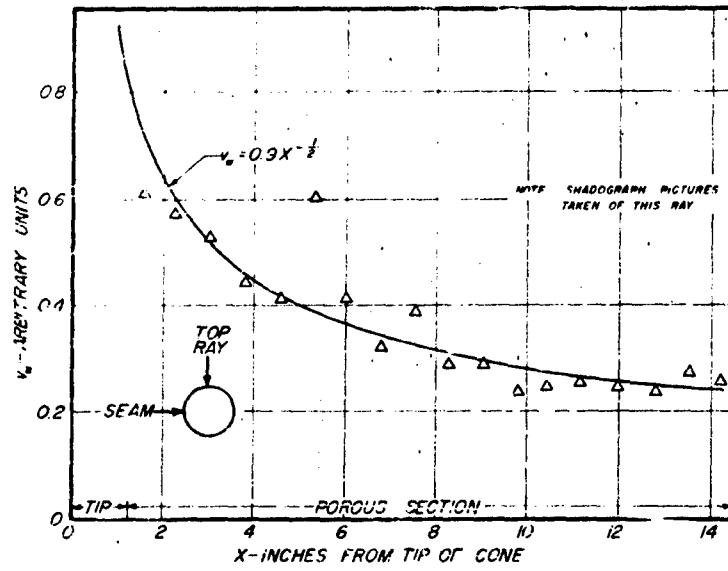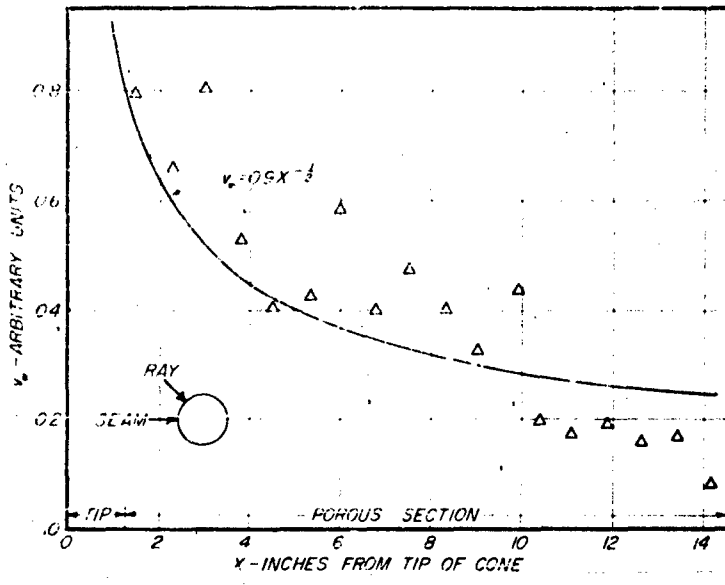
FIGURE 16b

FIGURE 15

FIGURE 16

FIGURE 165
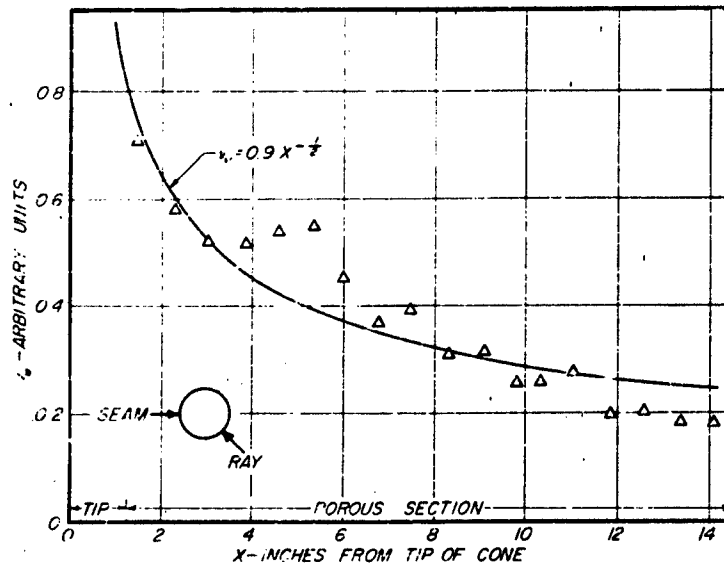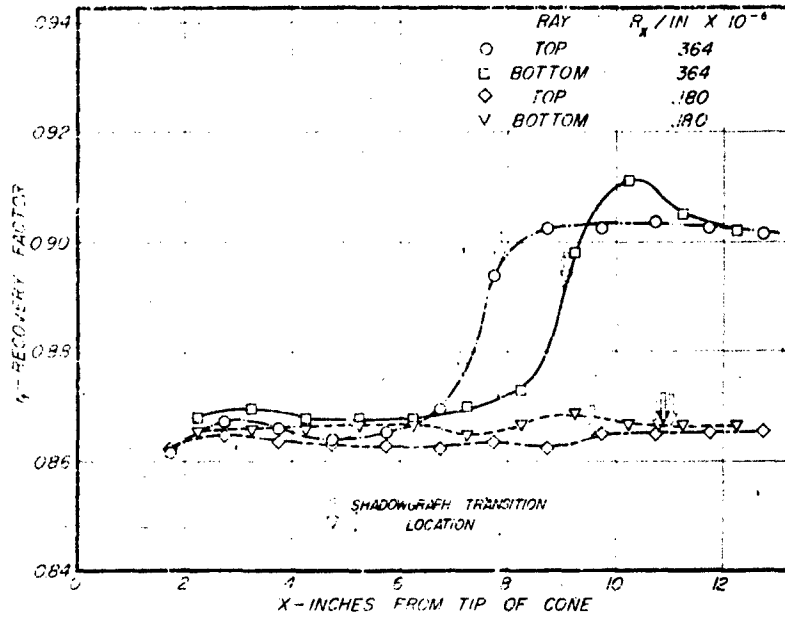
FIGURE 166

FIGURE 17. THE TEMPERATURE RECOVERY FACTOR DISTRIBUTION AT ZERO INJECTION.
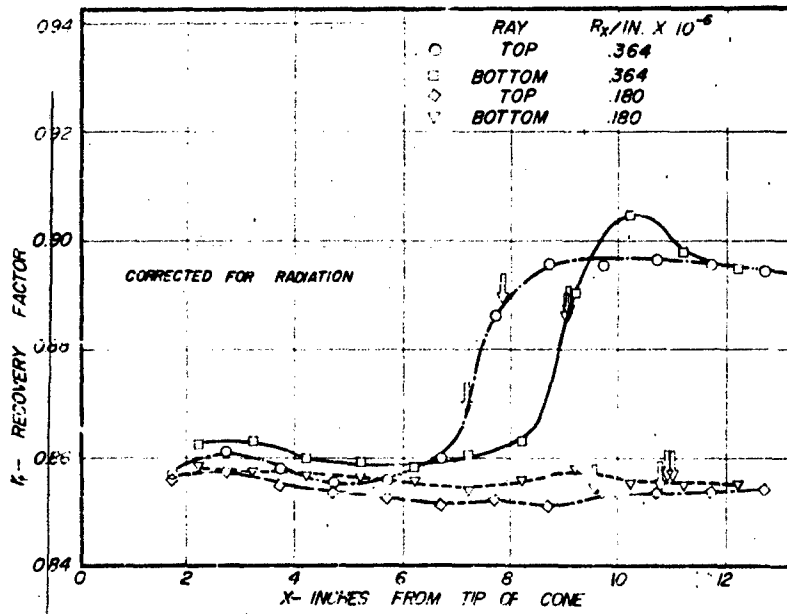
FIGURE 18. THE TEMPERATURE RECOVERY FACTOR DISTRIBUTION, CORRECTED FOR RADIATION.
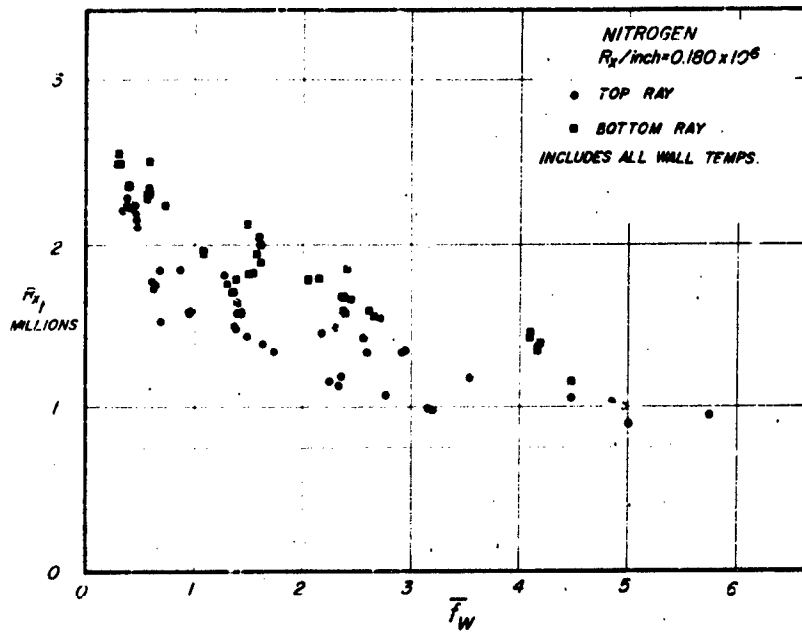
FIGURE 19. THE REDUCTION OF TRANSITION WITH NITROGEN INJECTION - HEAT TRANSFER MODEL.
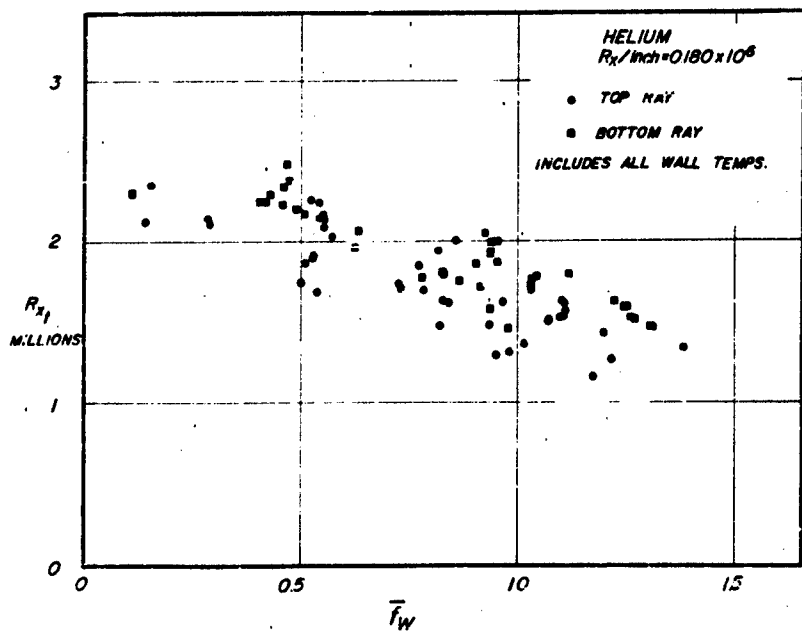
FIGURE 20. THE REDUCTION OF TRANSITION WITH HELIUM INJECTION - HEAT TRANSFER MODEL.
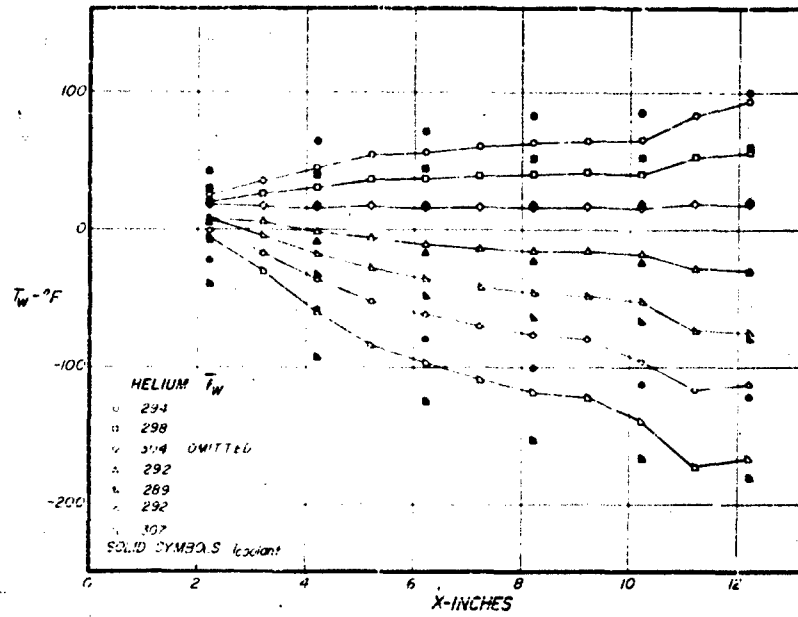
FIGURE 21A SURFACE TEMPERATURE DISTRIBUTION WITH HELIUM INJECTION.
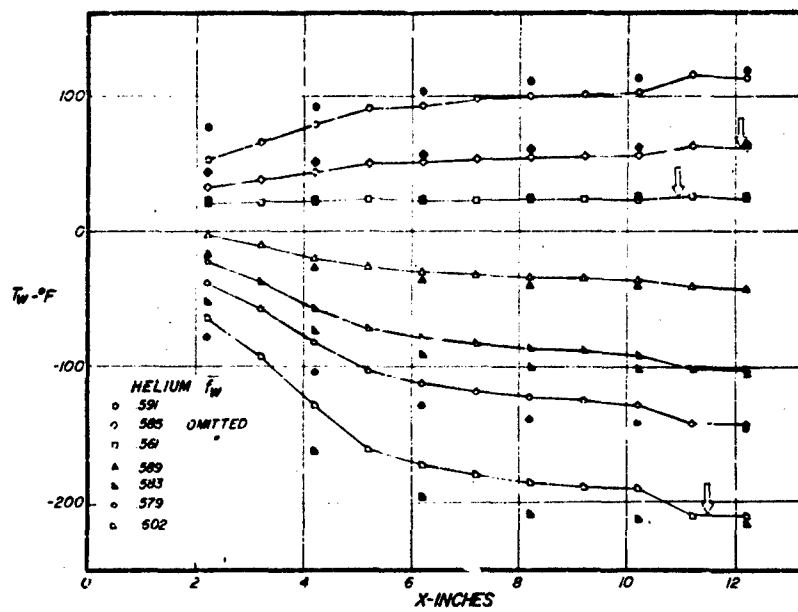
FIGURE 21B
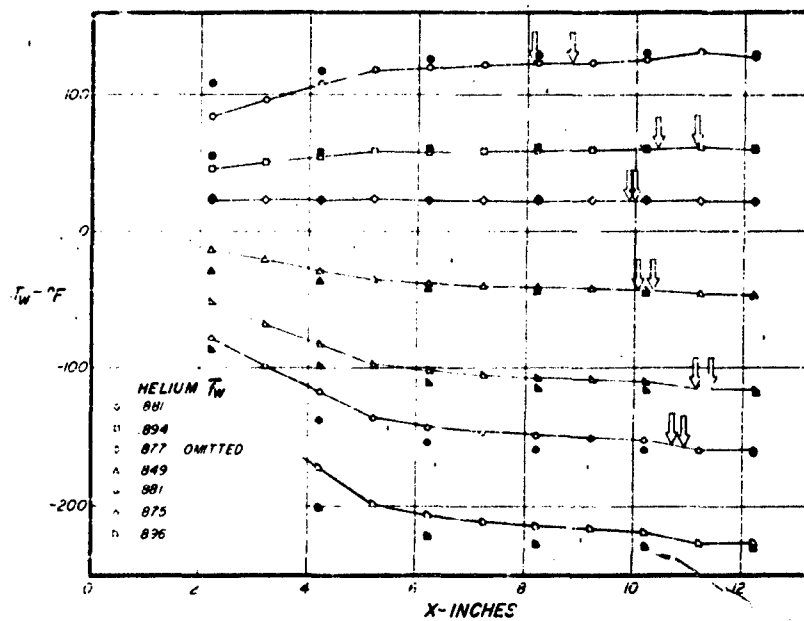
FIGURE 21c
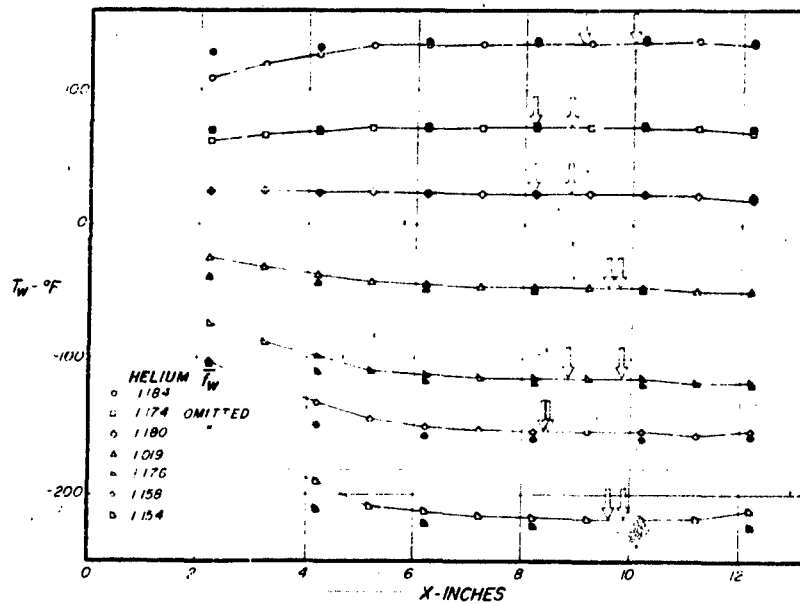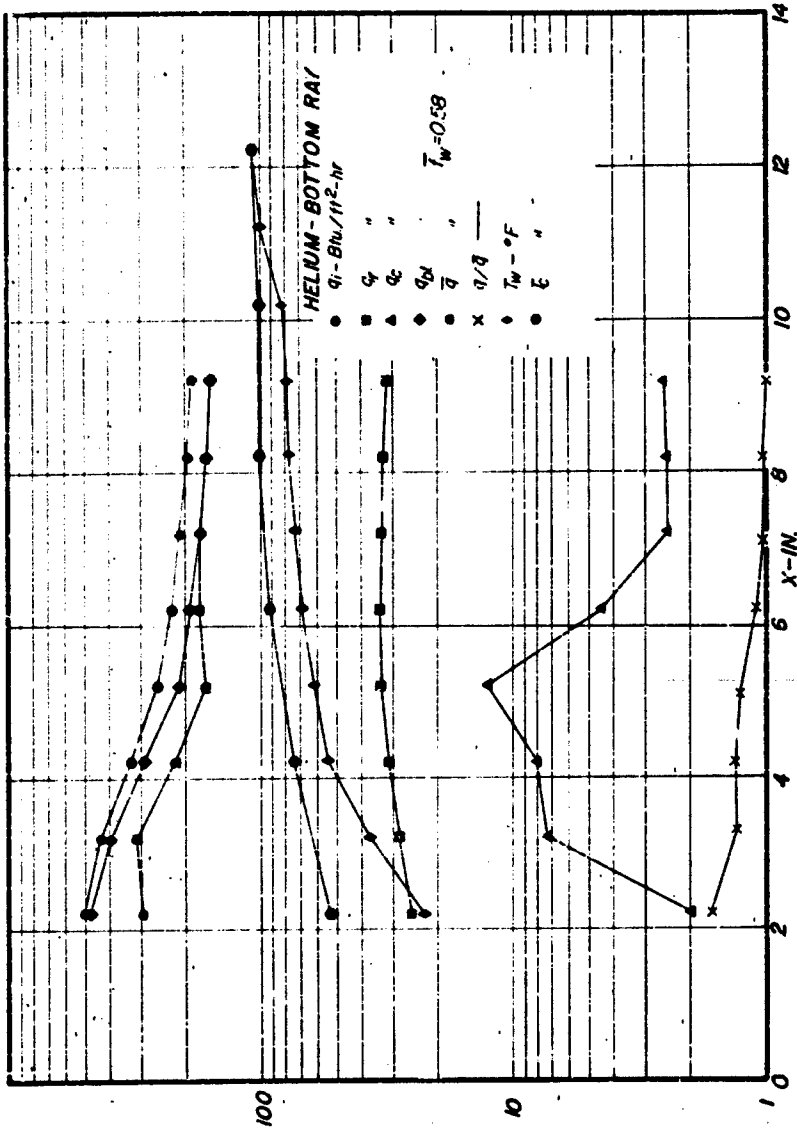
FIGURE 21

FIGURE 22. A PRESENTATION OF THE DATA FOR A TYPICAL TEST CONDITION - HELIUM INJECTION AT $\frac{z_s}{z_h} = 0.48$.
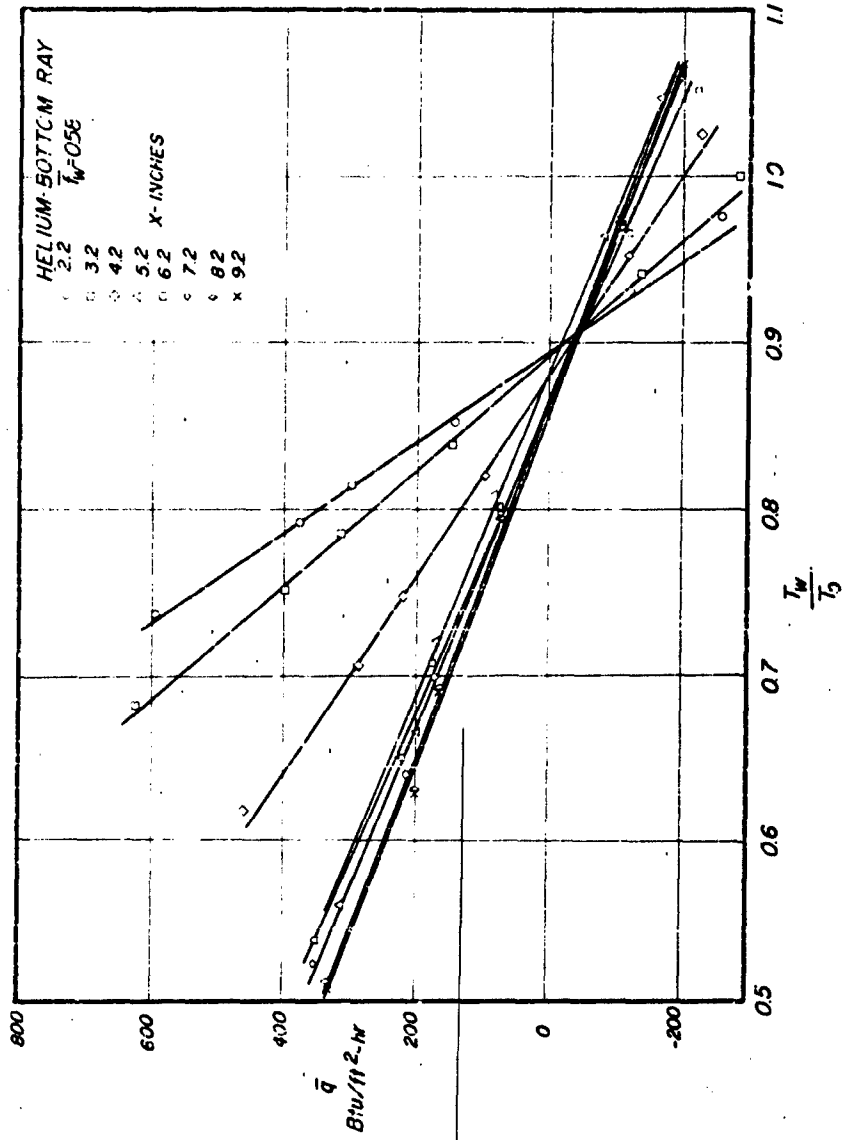
FIGURE 23. THE VARIATION OF SURFACE HEAT FLUX WITH WALL TEMPERATURE SHOWING AXIAL VARIATIONS WITH X.
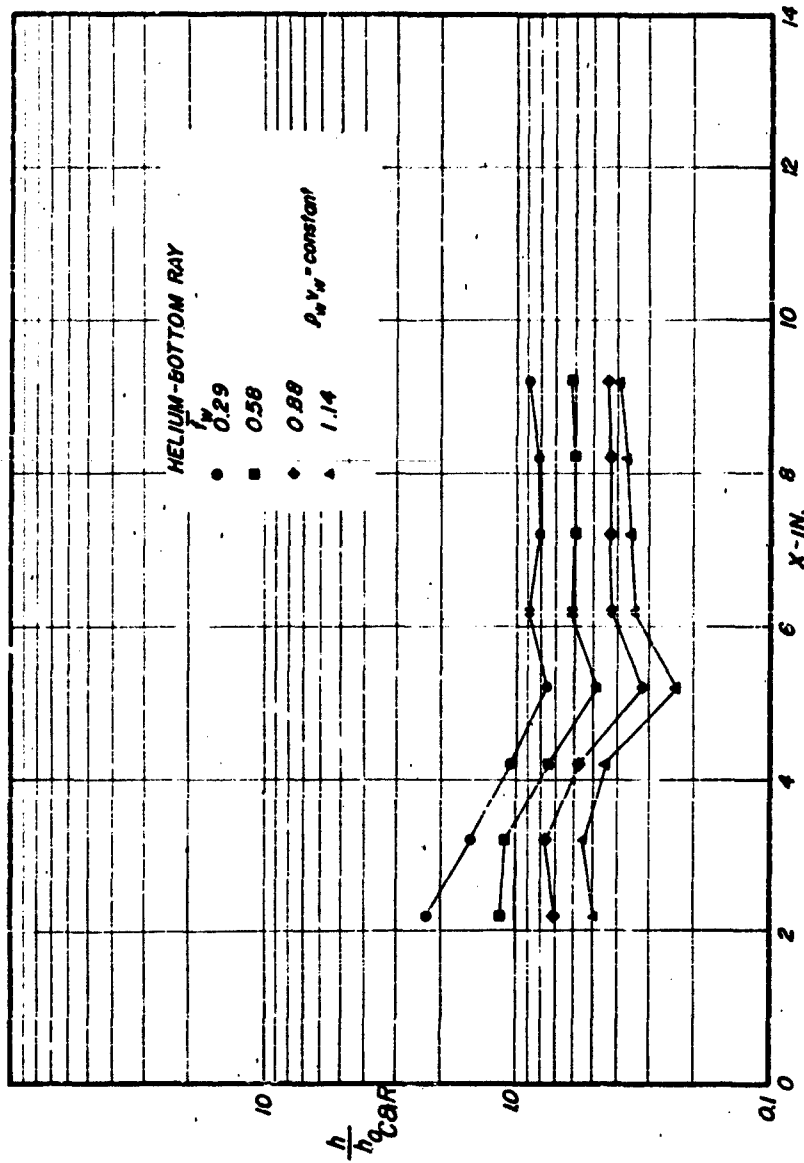
FIGURE 24. THE VARIATION OF THE DIMENSIONLESS HEAT TRANSFER COEFFICIENT WITH AXIAL POSITION FOR SEVERAL HELIUM INJECTION RATES.
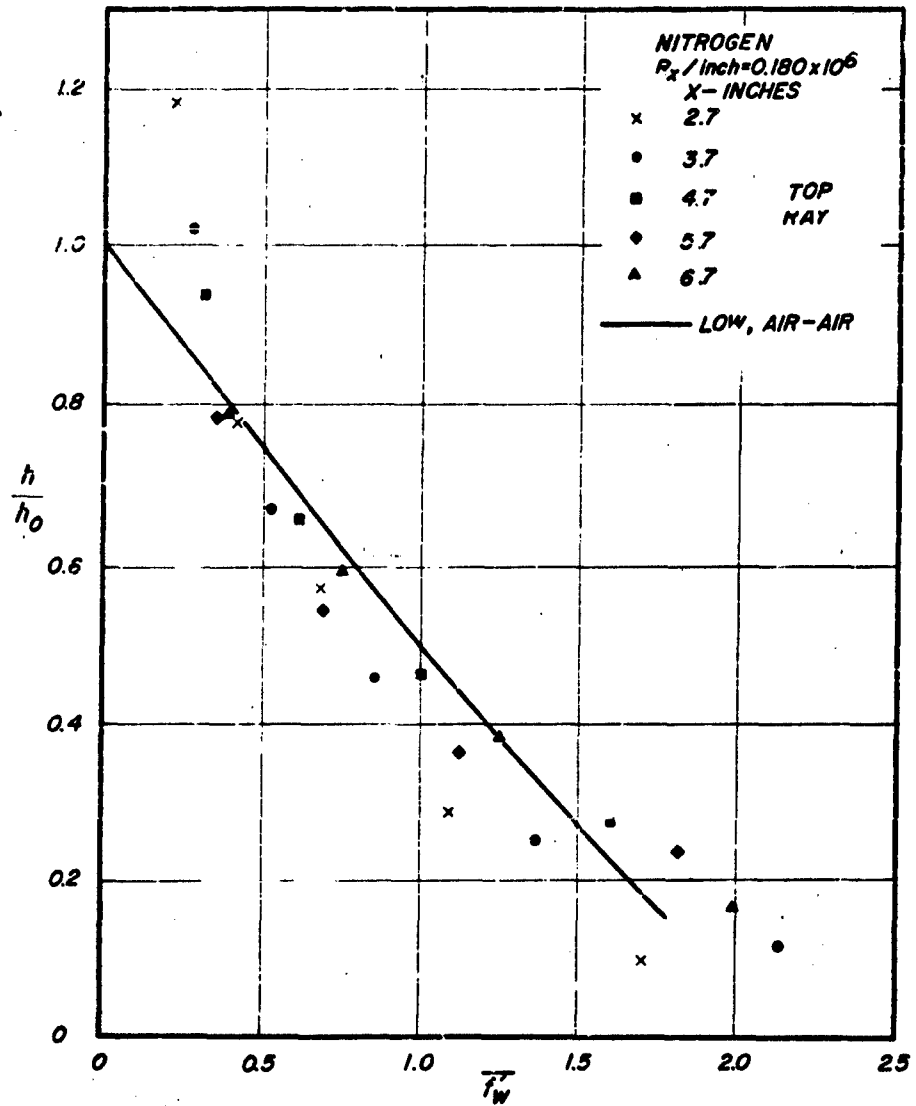
FIGURE 25. THE REDUCTION OF HEAT TRANSFER COEFFICIENT WITH NITROGEN INJECTION - TOP RAY
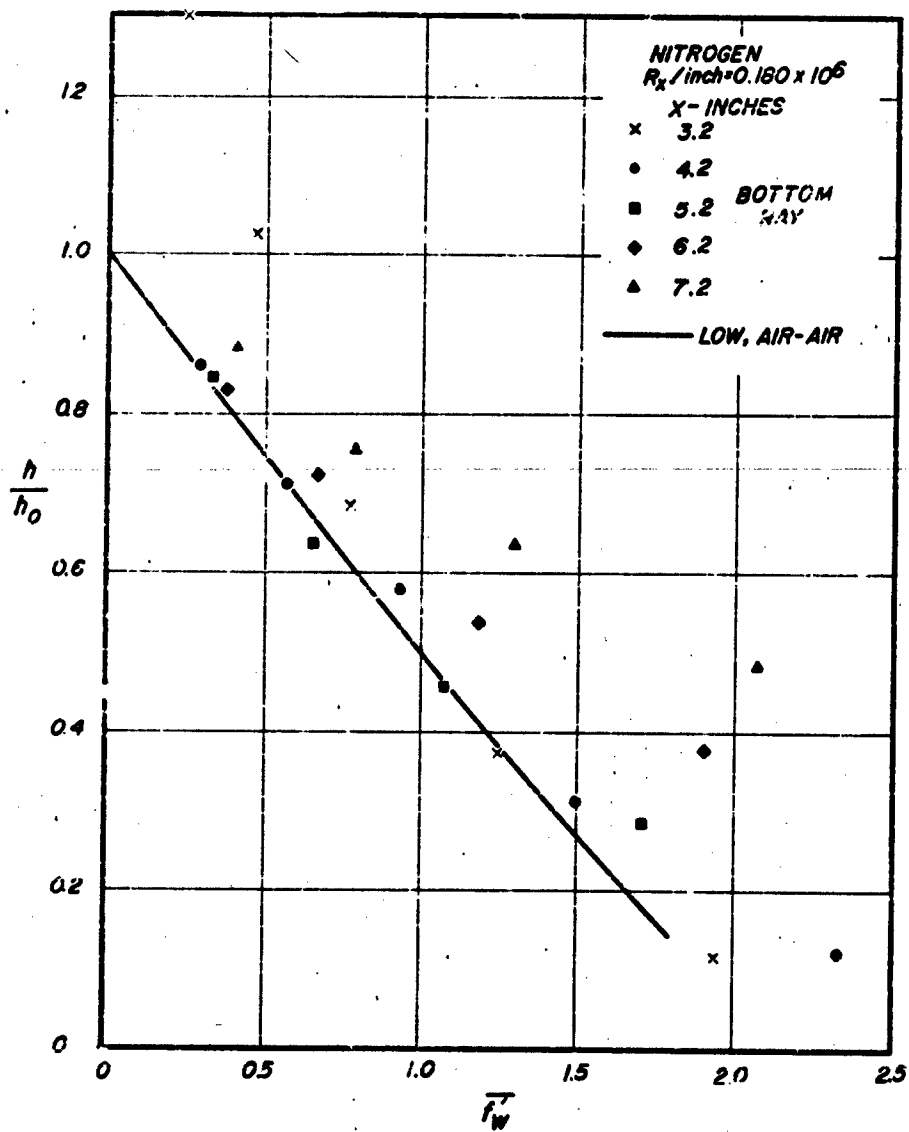
FIGURE 26. THE REDUCTION OF HEAT TRANSFER COEFFICIENT WITH NITROGEN INJECTION - BOTTOM RAY.
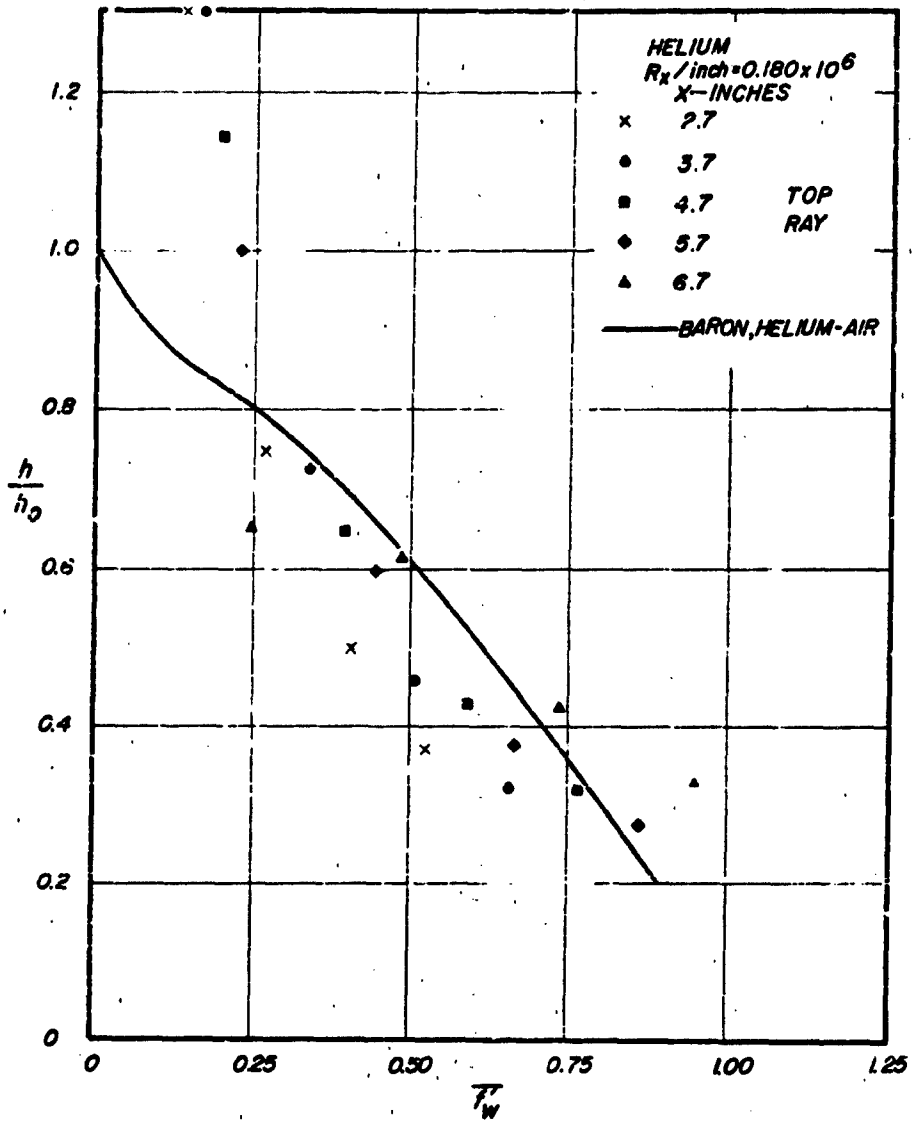
FIGURE 27. THE REDUCTION OF HEAT TRANSFER COEFFICIENT WITH HELIUM INJECTION - TOP RAY.
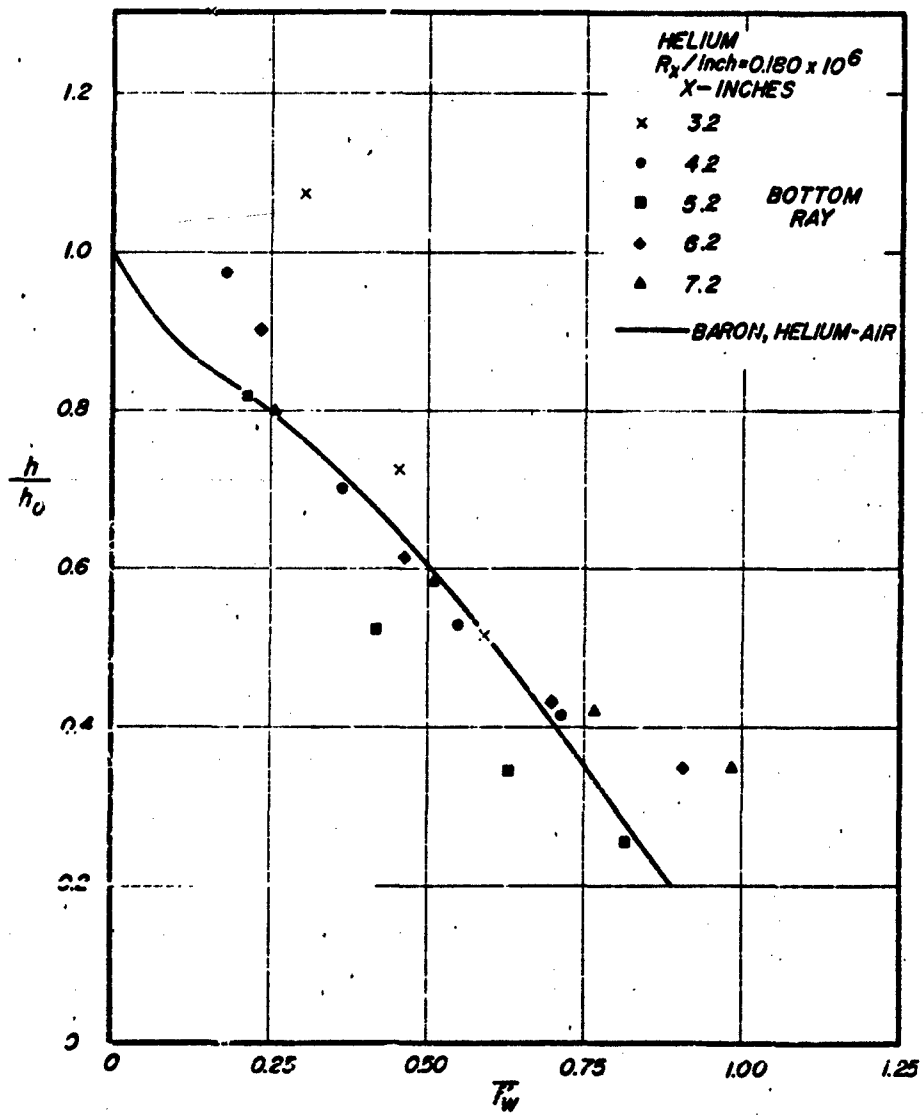
FIGURE 28. THE REDUCTION OF HEAT TRANSFER COEFFICIENT WITH HELIUM INJECTION - BOTTOM RAY.
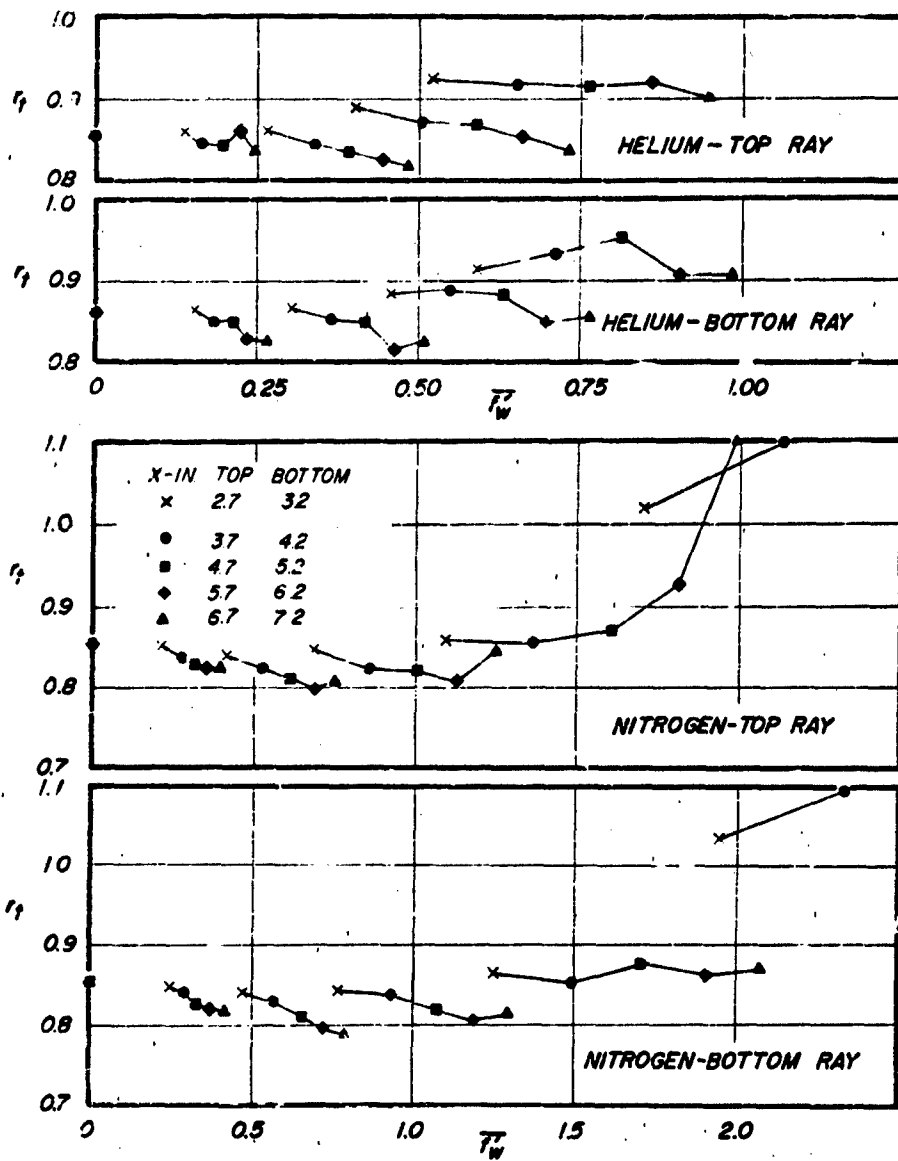
FIGURE 29. THE VARIATION OF TEMPERATURE RECOVERY FACTOR WITH INJECTION HELIUM AND NITROGEN INJECTION.
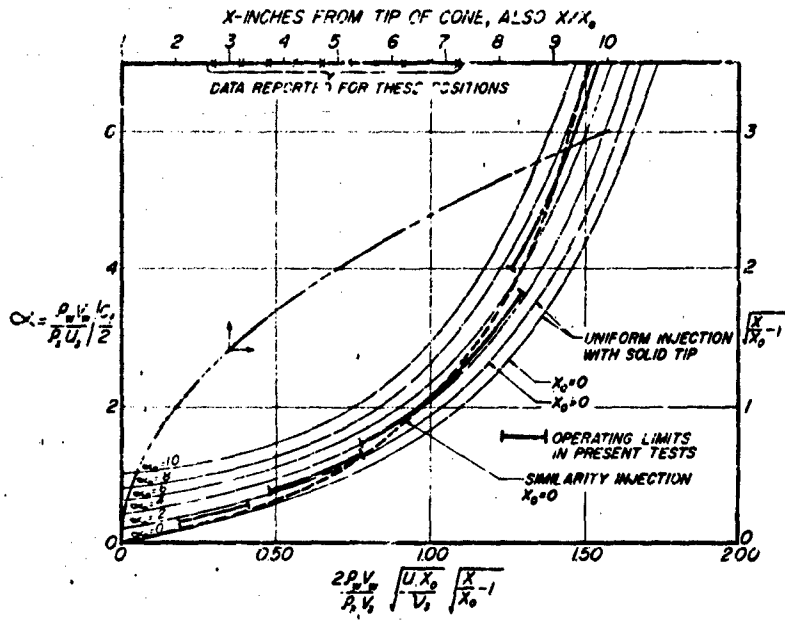
FIGURE 30. A COMPARISON OF THE THEORETICAL PREDICTIONS FOR UNIFORM AND SIMILARITY INJECTION.
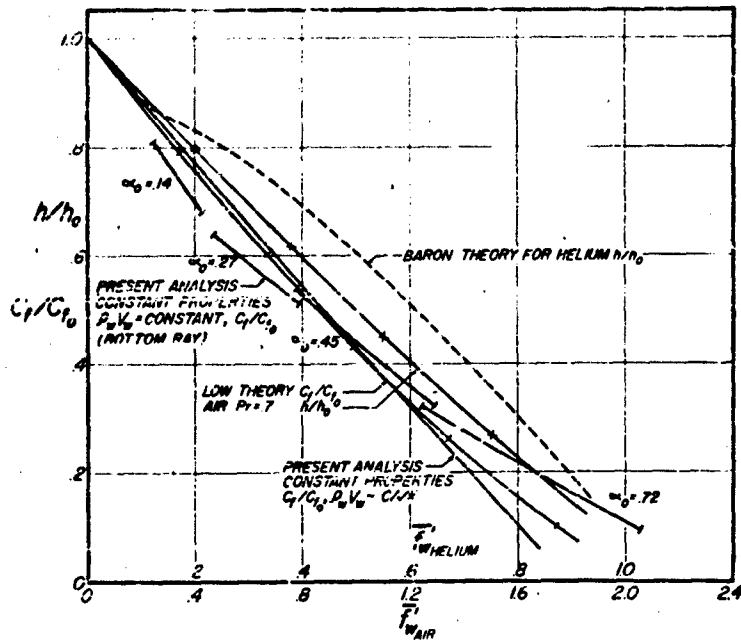
FIGURE 31. A COMPARISON OF THE THEORETICAL PREDICTIONS FOR UNIFORM AND SIMILARITY INJECTION - A COMPARISON OF SKIN FRICTION AND HEAT TRANSFER RESULTS.
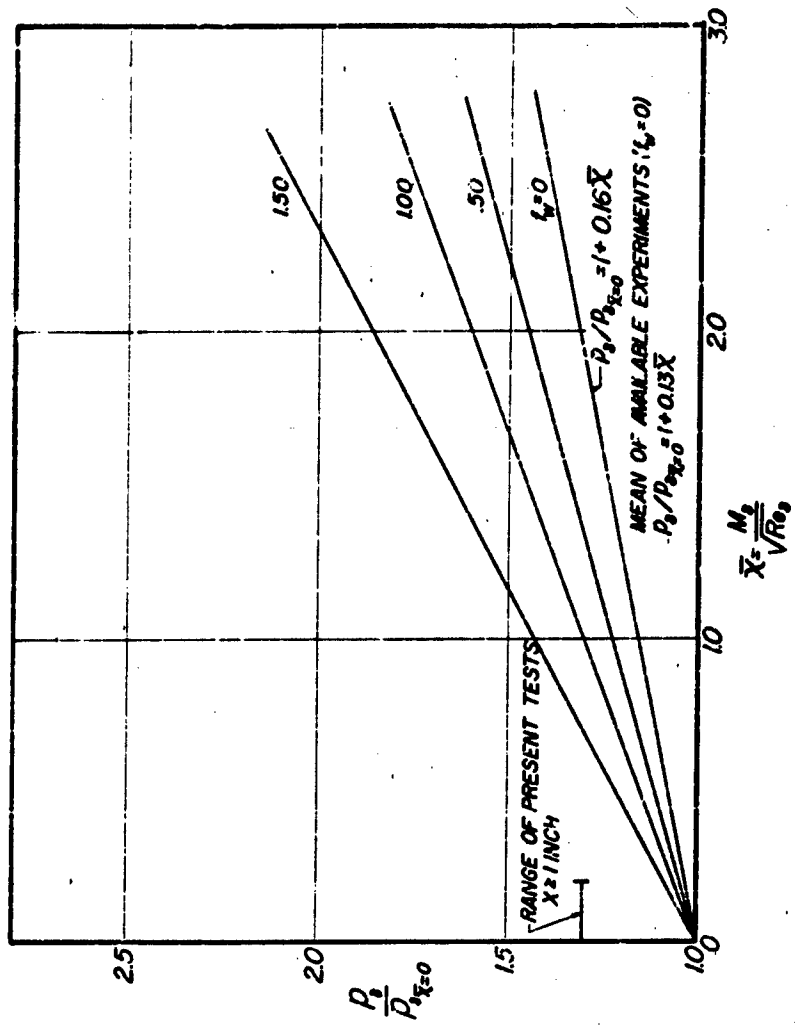
FIGURE 32. WEAK INTERACTION INDUCED PRESSURE ON AN ADIABATIC CONE.

FIGURE 33. LOW PRESSURE PERMEABILITY CALIBRATION APPARATUS.

0   0.010   0.020"

Average RMS roughness ≅ 60μ"
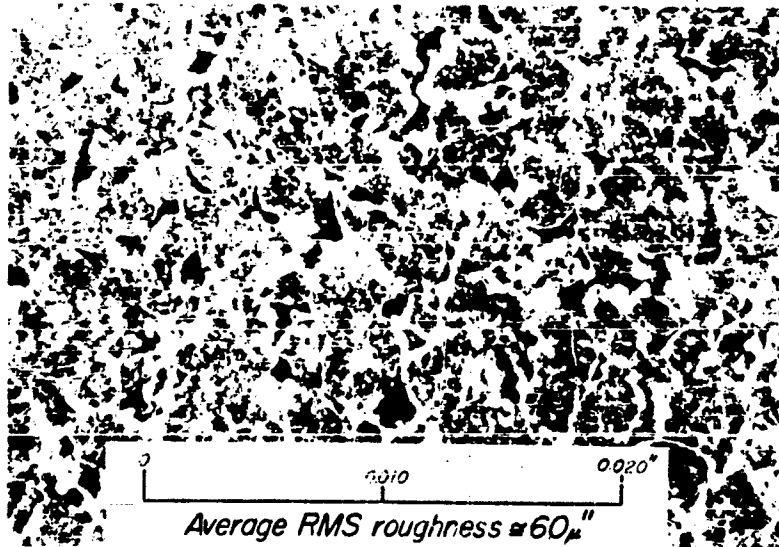
FIGURE 34. PHOTOMICROGRAPH OF POROUS CONE SURFACE.
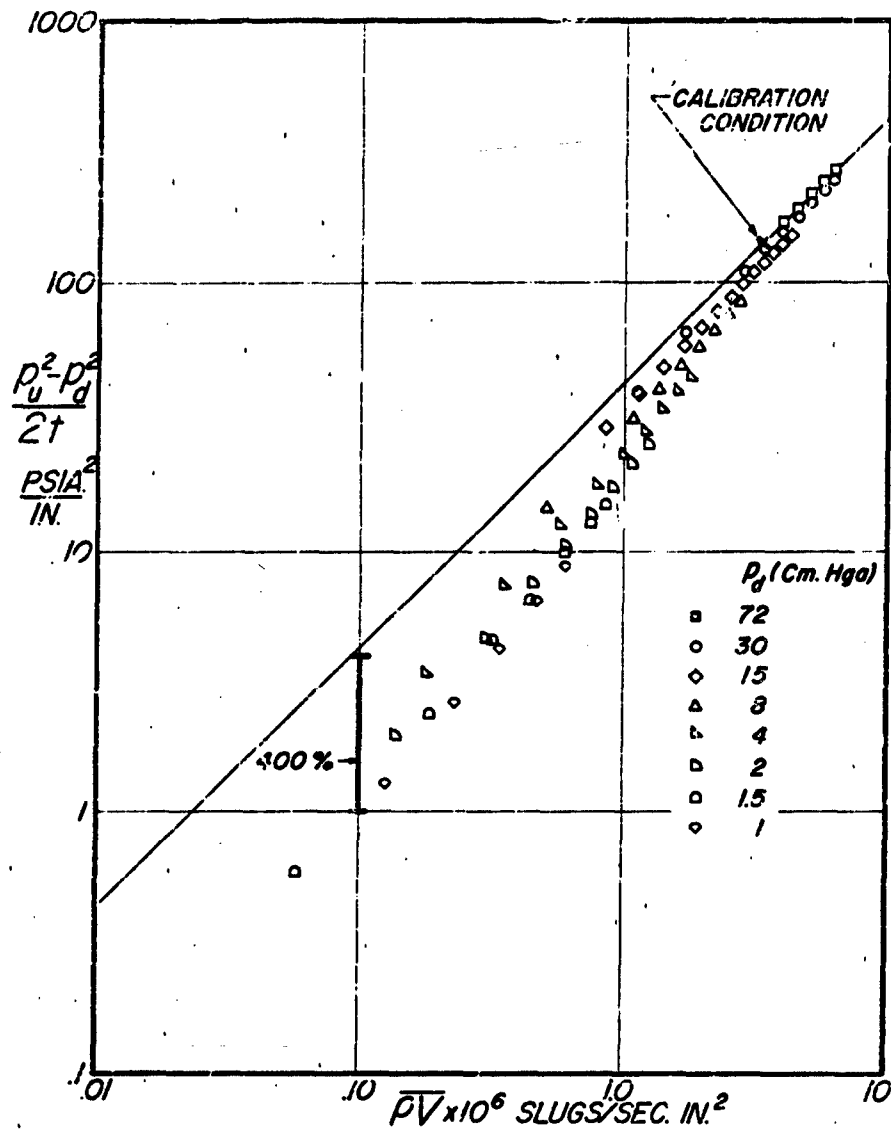
FIGURE 35. PRESSURE-SQUARE GRADIENT VS MASS FLUX RATE AT SEVERAL CHANNEL PRESSURES.
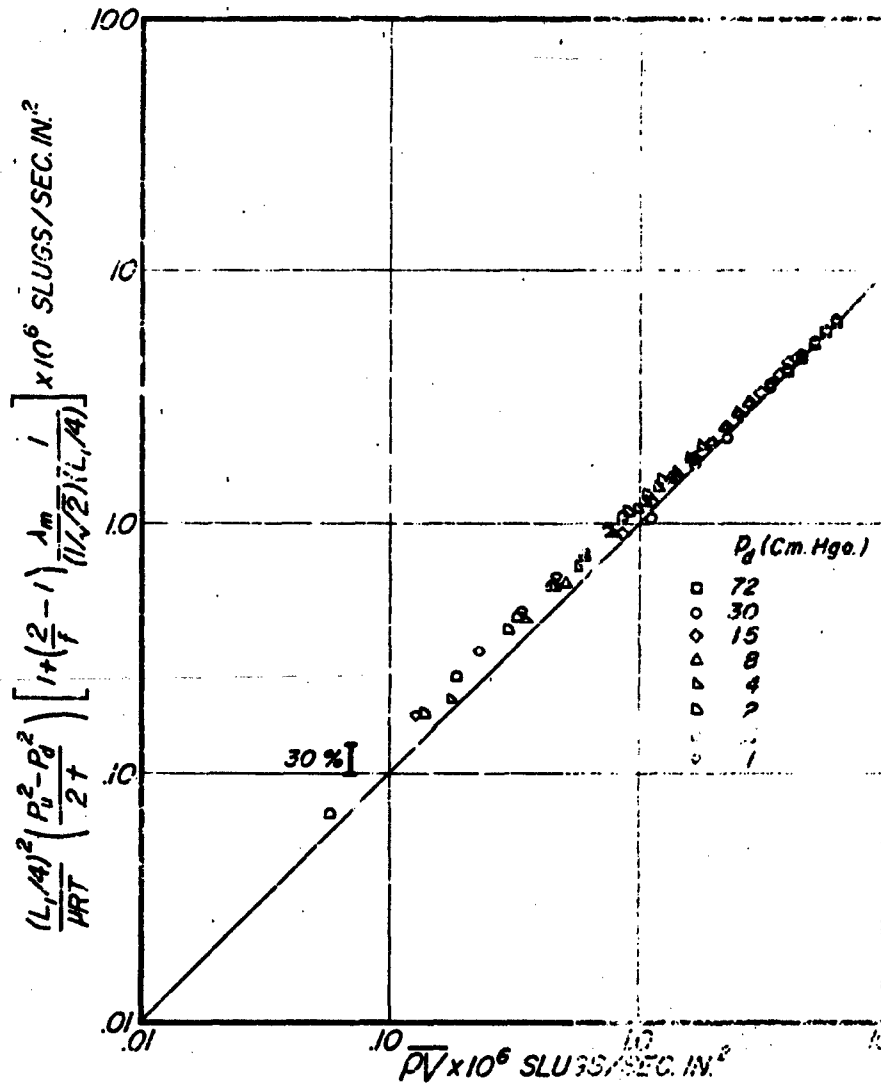
FIGURE 36.   CORRELATION OF LOW PRESSURE PERMEABILITY DATA.

UNCLASSIFIED